

---

# Back to Parsimonious Latents: Learning Task-Centric World Models from Visual Foundations

---

Minghao Fu<sup>1</sup> Fan Feng<sup>1</sup> Nicklas Hansen<sup>1</sup> Biwei Huang<sup>1</sup>  
<sup>1</sup>University of California, San Diego  
 {m9fu, f2feng, nihansen, bih007}@ucsd.edu

## Abstract

World models enable agents to predict future dynamics conditioned on actions, making the choice of latent representation central to planning and control. Such representations are often either learned directly from pixels with limited semantic structure or inherited from frozen visual foundation models with excessive task-irrelevant detail, yielding state spaces that are poorly matched to downstream planning and control. This is especially challenging in reward-free offline settings, where the model must learn from fixed trajectories without reward supervision or online interaction. To address this, we propose TC-WM, a framework for turning foundation-model embeddings into compact, task-sufficient world representations. The key design is to treat the pretrained embedding space as a semantic scaffold rather than as the final state space: TC-WM linearly projects high-dimensional visual embeddings into a compact latent as the dynamic space, aligns a subspace with the agent’s physical state via contrastive learning, and reconstructs embeddings to preserve useful visual structure. This combines the generality of foundation features with the controllability of task-centric dynamics. Theoretically, we show that TC-WM suffices to identify the underlying task-centric latent factors up to a simple transformation. Empirically, TC-WM enables test-time planning across diverse environments (*e.g.*, Robomimic and D4RL), achieving better world-modeling quality and more precise control than state-of-the-art approaches.

**Webpage:** <https://minghaofu.com/tc-wm/>

## 1 Introduction

An agent that can simulate its environment can plan, generalise, and act efficiently from limited experience, a long-standing goal that motivates research on *world models* [Sutton, 1991, Ha and Schmidhuber, 2018, Hafner et al., 2020, Hansen et al., 2024]. Recent progress has crystallised the field into three architectural branches that differ in the level at which dynamics are predicted (Figure 1). **Generative** models (a) predict future observations directly in pixel space [Ha and Schmidhuber, 2018], providing rich visualisation but at heavy computational cost. **Latent** models (b) instead learn a compact latent representation and predict dynamics within it [Hafner et al., 2021, 2023, 2025, Hansen et al., 2022, 2024, Schrittwieser et al., 2020], with reward signals (*e.g.*, in TD-MPC and MuZero) often shaping the latent into a task-relevant representation. **Embedding** models (c), most recently exemplified by DINO-WM and V-JEPA [Assran et al., 2025, Zhou et al., 2025, Baldassarre et al., 2025], skip the representation-learning step by predicting directly in the frozen feature space of a pre-trained foundation model, leveraging its broad semantic priors for zero-shot generalisation.

Generally, pretrained visual embeddings are useful not because they form ideal state representations, but because they provide a strong semantic coordinate system from which such states can be extracted. This view is aligned with recent representation-alignment results in generative modelling (*e.g.*, REPA [Yu et al., 2025]), which shows that tying generative latents to frozen visual encoders simplifies high-dimensional generation. For world models, we therefore build dynamics *on top of*

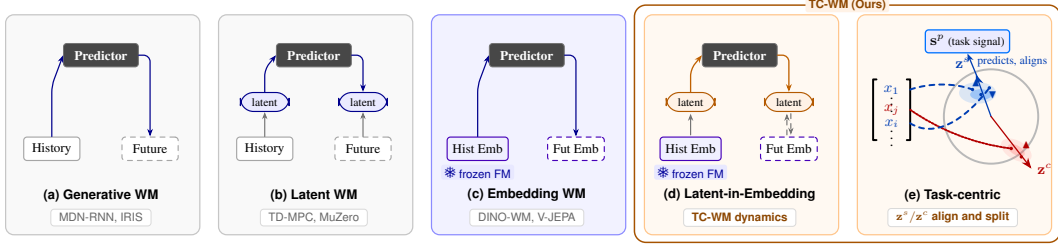


Figure 1: Comparison of world model paradigms (a)–(c) and our task-centric refinement (d)–(e). Detailed related work can be found in Section D.

foundation embeddings rather than from pixels alone, inheriting object- and scene-level structure before learning temporal prediction.

The challenge is that foundation embeddings are optimised for broad semantic coverage rather than for world dynamics or specific planning tasks [Hafner et al., 2020, Hu et al., 2023, Zhang et al., 2025]: they encode textures, lighting, and background details that do not affect control. A robot navigating a room needs spatial layout and movable-object dynamics, not wall colour or sofa texture. When generic embeddings serve directly as world-model latents, the model spends capacity on irrelevant variation, hurting modelling efficiency and control interpretability [Schneider et al., 2024]. This burden is most acute under *high-dimensional action spaces*: Maze or Push-T use only 2-D actions, but contact-rich Robomimic requires a 7-DoF arm with a 43-D proprioceptive state (Table A1), where every irrelevant latent dimension becomes a possible factor of representation-collapse and wasted planning capacity. The task-centric fix, pursued broadly in representation learning [Lesort et al., 2018, Schölkopf et al., 2021, Locatello et al., 2020, Ho et al., 2022] and implemented by reward-guided latents in, e.g., TD-MPC2 and MuZero [Hansen et al., 2024, Schrittwieser et al., 2020], is to retain only the information needed to predict task-relevant futures.

We introduce TC-WM (Figure 1d–e), a task-centric world model designed around this decomposition. Instead of predicting pixels or rolling out the full foundation embedding, TC-WM treats the embedding as a reusable visual scaffold and learns compact latent dynamics above it. A designated subspace aligns with the environment’s physical state, while the complementary subspace remains anchored to the pretrained embedding via reconstruction, preserving useful visual structure while filtering nuisance variation. This design yields an *identifiability* guarantee of task-relevant representation of world dynamics, validated by our linear probing and ablations.

Once the task-centric representation is ready, it supports *a wide suite of* downstream policy-learning control, including test-time planning with model predictive control [Draeger et al., 1995] for goal-reaching tasks, a latent diffusion planner [Xie et al., 2025] for manipulation tasks, and model-free reinforcement learning [Haarnoja et al., 2018] for locomotion tasks.

Empirically, TC-WM improves both world model quality, reward-free offline planning and control across 9 benchmarks; Figure 2 highlights the Robomimic setting with a high-dimensional action space, where the gains are largest, the learned latent linearly recovers physical states, and our design prevents representation collapse compared with models directly building on visual embeddings.

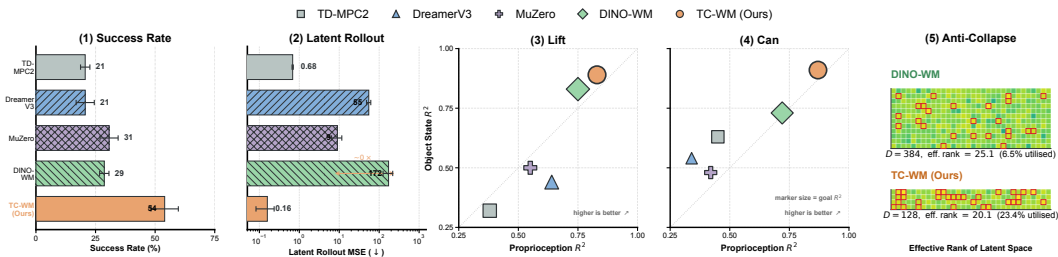


Figure 2: Experiment results on Robomimic. (1) Success rate. (2) Latent-rollout MSE. (3)–(4) Linear probes on Lift and Can. (5) Anti-collapse: TC-WM has better utilisation of latent space.

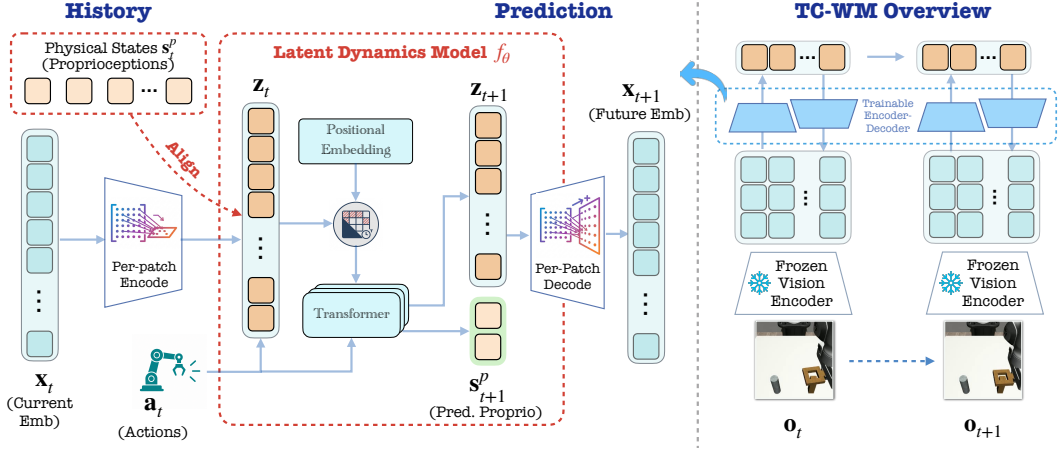


Figure 3: We present **TC-WM**, a method for training a world model by extracting a compact, task-centric latent dynamics from pretrained visual embeddings of image frames using the task-centric side information, *e.g.*, proprioception.

## 2 Method

### 2.1 Problem Setup

We formulate the problem as a partially observable Markov decision process (POMDP) [Kaelbling et al., 1998] defined by  $(\mathcal{S}, \mathcal{O}, \mathcal{A}, p_{\text{env}})$ , where  $\mathcal{S}$  denotes the latent environment state space,  $\mathcal{O}$  the observation space, and  $\mathcal{A}$  a continuous action space. The environment evolves according to latent dynamics  $p_{\text{env}}(s_{t+1} | s_t, a_t)$ , while observations  $o_t \in \mathcal{O}$  are generated from latent states  $s_t$  through an unknown observation process. We assume access to a low-dimensional *proprioceptive* signal  $s_t^p \in \mathbb{R}^d$ , which captures the agent’s physical configuration (*e.g.*, joint positions, end-effector pose, gripper state). This signal represents a partial, directly observable projection of the full state  $s_t$ .

Given an offline dataset of visual trajectories  $\mathcal{D} = \{(o_t, a_t, s_t^p)\}_{t=0}^T$ , where visual observations can be further encoded into embeddings  $x_t$ , our goal is to learn a world model that infers a latent representation  $z_t$  from observation histories and models its dynamics. We aim for the learned latent sequence  $[z_0, \dots, z_T]$  to be *task-centric*, meaning that it preserves information necessary to predict future task-relevant dynamics under actions, which is formally defined below.

**Definition 1** (Task-Centric Representation). *A latent representation  $z_t = f(o_{\leq t}, a_{< t})$  is task-centric with respect to proprioceptive state  $s_t^p$  if it satisfies the following two conditions.*

$$\underbrace{p_{\text{env}}(s_{t+H}^p | o_{\leq t}, a_{< t}, a_{t:t+H-1}) = p_{\text{env}}(s_{t+H}^p | z_t, a_{t:t+H-1})}_{\text{Sufficiency: for any action sequence replacing history by } z_t \text{ leaves the future unchanged}} \quad \underbrace{p_{\text{env}}(s_t^p | z_t) = p_{\text{env}}(s_t^p | o_{\leq t}, a_{< t})}_{\text{Task-Aligned: preserve the current proprioceptive state}}$$

### 2.2 Task-Centric World Model (TC-WM)

**Overview.** TC-WM learns a compact rollout state  $z_t$  on top of frozen visual embeddings, using proprioception to identify the dimensions needed for physical dynamics. Figure 3 illustrates the pipeline, whose main components are:

Joint embedding	$x_t = [f_{\text{emb}}^o(o_t), f_{\text{emb}}^p(s_t^p)]$	▷ Frozen visual + trainable proprio
Latent encoder	$z_t \sim q(z_t   x_t)$	▷ Linear projection to compact latent
TC alignment	$z_t^s \leftrightarrow s_t^p, z_t = [z_t^s, z_t^c]$	▷ Align $z^s$ with proprio
Latent dynamics	$\hat{z}_{t+1} = f_\theta(z_{t-H:t}, a_{t-H:t})$	▷ Predicts next latent state
TC dynamics	$\hat{s}_{t+1}^p = f_\eta^p(z_{t-H:t}, a_{t-H:t})$	▷ Predicts next proprioception
Embedding decoder	$\hat{x}_t = f_{\text{dec}}(z_t)$	▷ Reconstructs visual embedding

(1)

Here  $H$  is the prediction horizon,  $\mathbf{o}_t$  the image observation, and  $\mathbf{s}_t^p$  the observed proprioceptive signal. The embedding  $\mathbf{x}_t$  serves as the visual anchor, while  $\mathbf{z}_t$  is the latent state optimised for prediction and planning. We introduce each module below.

▷ **Joint Embedding.** At each time step, a frozen encoder  $f_{\text{emb}}^o$ , such as DINOv2 [Oquab et al., 2023], maps the image  $\mathbf{o}_t$  to a visual feature, while a trainable linear layer  $f_{\text{emb}}^p$  maps proprioception  $\mathbf{s}_t^p$ . Their concatenation  $\mathbf{x}_t = [f_{\text{emb}}^o(\mathbf{o}_t), f_{\text{emb}}^p(\mathbf{s}_t^p)]$  is not the rollout state. It provides a structured input to the latent encoder: frozen visual features contribute spatially coherent, object-centric cues [Zhou et al., 2025, Baldassarre et al., 2025, Yu et al., 2025], and proprioception supplies the physical coordinate injection, which serves as side information.

▷ **Latent Encoder.** To further distill the visual embeddings, TC-WM treats them as a scaffold rather than directly modeling temporal dynamics within them. Specifically, we introduce an encoder  $q(\mathbf{z}_t | \mathbf{x}_t)$  that transforms the joint embedding  $\mathbf{x}_t$  into a latent representation  $\mathbf{z}_t$ , which is further trained to satisfy Definition 1. This projection is the central abstraction step: it retains the semantic directions useful for reconstructing and predicting the scene, but compresses away dimensions that are not useful for future physical state prediction.

▷ **TC Alignment.** Directly aligning the full latent space with  $\mathbf{s}^p$  would discard the rich semantic content captured by the visual embedding. We therefore perform a *partial* alignment: we factorise  $\mathbf{z}_t = [\mathbf{z}_t^s, \mathbf{z}_t^c]$  and align only the state-relevant block  $\mathbf{z}_t^s$  with the proprioceptive state  $\mathbf{s}_t^p$  via an InfoNCE-style contrastive objective [Oord et al., 2018], leaving the complementary block  $\mathbf{z}_t^c$  free to absorb residual semantic structure (object appearance, background, etc.) so that the embedding-reconstruction loss introduced below can still be satisfied. Critically, this contrastive term plays a stronger role than mere prediction: prior conditional generative identifiability frameworks [Khemakhem et al., 2020, Zimmermann et al., 2021] *passively assume mechanism diversity*, that is, distinct physical states inducing distinct conditionals, as a property of the data-generating process. TC-WM’s alignment instead *actively produces* this diversity on  $\mathbf{z}_t^s$  by pushing latents tied to different proprioceptive states apart, turning what was a passive assumption (cf. A2 of Theorem A1) into a learned property of the encoder.

$$\mathcal{L}_{\text{align}} = -\log \frac{\exp(\text{sim}(g_\phi(\mathbf{z}_t^s), h_\psi(\mathbf{s}_t^p))/\tau)}{\sum_{\mathbf{s}_t^-} \exp(\text{sim}(g_\phi(\mathbf{z}_t^s), h_\psi(\mathbf{s}_t^{p-}))/\tau)}, \quad (2)$$

where  $g_\phi, h_\psi$  are small projection heads,  $\text{sim}(\cdot, \cdot)$  is cosine similarity,  $\tau$  is the temperature, positive pairs  $(\mathbf{z}_t^s, \mathbf{s}_t^p)$  are drawn from the same timestep, and negatives  $\mathbf{s}_t^{p-}$  from other samples in the batch. In practice,  $g_\phi$  is implemented as a *linear* map  $\mathbb{R}^{d_z} \rightarrow \mathbb{R}^{d_s}$  with an  $\ell_1$  penalty on its weight matrix, so  $\mathbf{z}_t^s$  is automatically *selected* by sparsity rather than pre-sliced from  $\mathbf{z}_t$ ;  $d_s$  functions only as an upper bound on the width of the task-centric block.

▷ **Latent Dynamics.** We adopt the ViT [Dosovitskiy, 2020] as the transition architecture  $f_\theta$  to predict  $\hat{\mathbf{z}}_{t+1} = f_\theta(\mathbf{z}_{t-H:t}, \mathbf{a}_{t-H:t})$ , which models the temporal dependencies of states and actions by minimizing a predictive consistency loss

$$\mathcal{L}_{\text{dyn}}^z = \|\hat{\mathbf{z}}_{t+1} - q(\mathbf{z}_{t+1} | \mathbf{x}_{t+1})\|_2^2$$

which encourages the transition to capture dynamics in the projected latent space rather than at the raw embedding level.

▷ **TC Dynamics.** Beyond instantaneous alignment, we predict these proprioceptive variables directly from the history to encourage the latent space to capture task-centric dynamics:

$$\mathcal{L}_{\text{dyn}}^s = \|f_\eta^p(\mathbf{z}_{t-H:t}, \mathbf{a}_{t-H:t}) - \mathbf{s}_{t+1}^p\|_2^2.$$

We predict raw (but standardised) proprioception rather than its embedding, which avoids trivial solutions where the state-embedding layer  $f_{\text{emb}}^p$  collapses to match its own output.

▷ **Embedding Decoder.** A trainable linear decoder  $f_{\text{dec}}$  reconstructs the visual embedding  $\mathbf{x}_t$  from  $\mathbf{z}_t$ . This term acts as a *regulariser* that anchors the compact latent to the foundation-embedding

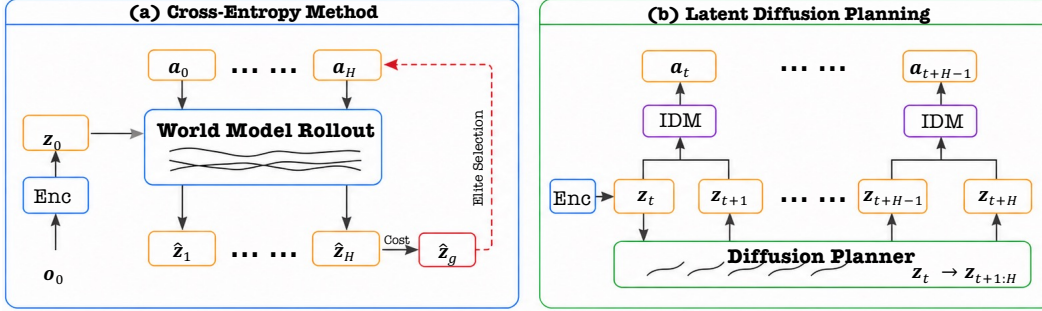


Figure 4: Planning algorithms used in TC-WM. **(a) Cross-Entropy Method (CEM)** for navigation: the world model rolls out  $K$  sampled action sequences, scores each rollout against a goal latent  $\mathbf{z}_g$  via cost  $\mathcal{C}$ , and refines the action distribution by elite selection. **(b) LDP planning** for manipulation: a diffusion planner generates future latent trajectories  $[\mathbf{z}_{t+1}, \dots, \mathbf{z}_{t+H}]$ , and an inverse dynamics model (IDM) recovers executable actions from consecutive latent pairs.

manifold, keeping the latent space smooth, well-spread across samples, and free of the degenerate solutions that compact latents are otherwise prone to:

$$\hat{\mathbf{x}}_t = f_{\text{dec}}(\mathbf{z}_t), \quad \mathcal{L}_{\text{rec}} = \|\hat{\mathbf{x}}_t - \mathbf{x}_t\|_2^2. \quad (3)$$

In our view, the embedding of a visual foundation model, *e.g.*, DINO [Oquab et al., 2023] or V-JEPA [Assran et al., 2023], can be a better reconstruction target than raw pixels (which generative world models typically use [Hafner et al., 2020, 2023, Alonso et al., 2024]): it offers a denoised supervision signal that promotes a stable, compact latent, as verified in Section 3.3.

**Visual Decoder.** For visualization *only*, an auxiliary decoder maps predicted embeddings to images,  $\hat{\mathbf{o}}_t = f_{\text{vis}}(\hat{\mathbf{x}}_t)$ , with  $\mathcal{L}_{\text{img}} = \|\hat{\mathbf{o}}_t - \mathbf{o}_t\|_2^2$  separated from world-model optimization.

The overall training objective combines dynamics prediction and representation alignment:

$$\mathcal{L}_{\text{all}} = \mathcal{L}_{\text{dyn}}^z + \mathcal{L}_{\text{dyn}}^s + \lambda_{\text{align}} \mathcal{L}_{\text{align}} + \lambda_{\text{rec}} \mathcal{L}_{\text{rec}},$$

where  $\lambda_{\text{align}}$  balances alignment and dynamics, and  $\lambda_{\text{rec}}$  governs the embedding reconstructions.

### 2.3 Test-Time Planning and Control with TC-WM

To validate whether the task-centric representations can be translated into better downstream planning, we evaluate the learned world model on visual goal-reaching tasks performed entirely in the latent space  $\mathcal{Z}$ . Given an initial observation  $\mathbf{o}_0$  and a goal observation  $\mathbf{o}_g$ , we encode them as  $\mathbf{z}_0 = q(\mathbf{z}_0 | \mathbf{x}_0)$  and  $\mathbf{z}_g = q(\mathbf{z}_g | \mathbf{x}_g)$ . Planning is then formulated as minimizing a latent-space objective that measures the distance between the predicted latent state and the goal state:

$$\mathcal{L}_{\text{plan}}(\mathbf{a}_{0:T}) = \|f_{\theta}^H(\mathbf{z}_0, \mathbf{a}_{0:T}) - \mathbf{z}_g\|_2^2.$$

For tasks with low-dimensional action spaces, such as *navigation*, we adopt model predictive control (MPC) [Draeger et al., 1995] with the cross-entropy method (CEM) to iteratively refine action sequences based on predicted rollouts by  $\mathcal{L}_{\text{plan}}(\mathbf{a}_{0:T})$  (Figure 4a). For high-dimensional, contact-rich *manipulation*, we use latent diffusion planning (LDP) [Xie et al., 2025] over TC-WM’s task-centric latents (Figure 4b). LDP trains a diffusion planner for future latent trajectories and an inverse dynamics model (IDM) for executable actions:

$$\mathcal{L}_{\text{LDP}}(\psi) = \mathbb{E}_{\tau, \epsilon} [\|\epsilon_{\psi}(\hat{\mathbf{z}}_{t+1:t+H}; \mathbf{z}_t, \tau) - \epsilon\|_2^2], \quad \mathcal{L}_{\text{IDM}}(\xi) = \mathbb{E}_{i, \tau, \epsilon} [\|\epsilon_{\xi}(\hat{\mathbf{a}}_{t+i}; \hat{\mathbf{z}}_{t+i}, \hat{\mathbf{z}}_{t+i+1}, \tau) - \epsilon\|_2^2].$$

At inference, the planner samples  $\hat{\mathbf{z}}_{t+1:t+H}$  by denoising conditioned on  $\mathbf{z}_t$ , and the IDM decodes actions from consecutive latent pairs. Compared with the original VAE-based LDP, replacing the encoder with TC-WM’s latent space gives a more structured representation for planning; details are in Appendix A.3. For continuous control, we couple TC-WM with an off-policy actor–critic. The resulting latent  $\mathbf{z}_t$  obtained by TC-WM is treated as the observation of a Soft Actor–Critic (SAC) agent [Haarnoja et al., 2018], which is then trained from environment interaction with the same protocol used by the baselines. We report the mean episode return across 3 seeds.

**Theoretical Rationale.** The following theorem formalizes why a compact latent learned on frozen embeddings, once aligned with physical signals, can recover the task-relevant state needed for prediction and planning. We write  $L_{\mathbf{v}|\mathbf{u}}$  for the conditional linear operator induced by  $p(\mathbf{v} | \mathbf{u})$ , where  $[L_{\mathbf{v}|\mathbf{u}}\phi](\mathbf{v}) = \int p(\mathbf{v} | \mathbf{u})\phi(\mathbf{u}) d\mathbf{u}$ . Injectivity of  $L$  means that distinct latent states induce distinguishable futures, i.e., the observed dynamics vary across latent states.

**Theorem 1 (Task-centric identifiability from visual embeddings)**

Suppose images  $\mathbf{o}_t$ , frozen embeddings  $\mathbf{x}_t$ , and latent variables  $\mathbf{z}_t = [\mathbf{z}_t^s, \mathbf{z}_t^c]$  follow the process in Section 2.2, and the learned latent world model matches the true joint distribution of adjacent embeddings  $\{\mathbf{x}_{t-1}, \mathbf{x}_t, \mathbf{x}_{t+1}\}$ . Assume:

**A1. (Contextual dynamics):**  $L_{\mathbf{x}_{t+1:t+H}|\mathbf{z}_t}$  and  $L_{\mathbf{x}_{t-H:t-1}|\mathbf{x}_{t+1:t+H}}$  are injective and bounded.

**A2. (Latent-observed variability):** For any  $\mathbf{z}_t^{(1)} \neq \mathbf{z}_t^{(2)}$ ,  $p(\mathbf{x}_t | \mathbf{z}_t^{(1)}) \neq p(\mathbf{x}_t | \mathbf{z}_t^{(2)})$ .

**A3. (Differentiability):** There exists a differentiable  $F$  such that  $F[p_{\mathbf{x}_t|\mathbf{z}_t}(\cdot | \mathbf{z}_t)] = h_z(\mathbf{z}_t)$ .

**A4. (Partial alignment):** The alignment objective in Eq. (2) is sufficiently minimized.

Then the learned  $\mathbf{z}_t$  is block-wise identifiable, and the task-centric  $\mathbf{z}_t^s$  is affine-identifiable:

$$\hat{\mathbf{z}}_t = h_z(\mathbf{z}_t), \quad h_z \text{ invertible and } C^1$$

**Latent Space Recovery:** the compact latent preserves the true world state up to reparameterization

$$\mathbf{z}_t^s = \mathbf{A}\hat{\mathbf{z}}_t^s + \mathbf{b}$$

**Task-Centric Recovery:** the aligned block recovers physical factors up to an affine map

*Proof sketch and intuition.* The observable joint distribution over neighboring embeddings determines an operator family that is a similarity transform of the diagonal operator indexed by  $p(\mathbf{x}_t | \mathbf{z}_t)$ . Injective context operators make this diagonalization unique up to a smooth reparameterization, and the alignment loss selects the task-centric block by tying it to physical variables. Thus, the linear projection and proprioceptive alignment in TC-WM can recover a compact, physically meaningful latent (see Appendix B) rather than only producing successful predictions on the training set.

### 3 Experiments

We evaluate TC-WM across a diverse set of offline control and visual planning benchmarks to assess whether the learned representations are *task-centric*, *predictively sufficient*, and effective for downstream decision-making. Our evaluation spans navigation, locomotion, and manipulation tasks across simulated and real-world settings. We focus on three complementary aspects: (i) the accuracy and stability of the learned world model, (ii) planning performance under both low- and high-dimensional action spaces, and (iii) the interpretability and structure of the learned latent representations through targeted ablations and analysis.

#### 3.1 Environments and Tasks

We evaluate TC-WM on 9 offline visual-control environments spanning *navigation*, *locomotion*, and *manipulation* in different metrics.

**Datasets.** As shown in Figure 5, the benchmark suite includes Maze and Wall for navigation, Push-T and RoboMimic Mandlekar et al. [2021] (Lift, Can, Square) for manipulation, and Reacher, Cheetah, and Hopper from DeepMind Control Suite [Tassa et al., 2018] for continuous control. Dataset construction, action/state dimensions, and preprocessing details are provided in Appendix A.1.

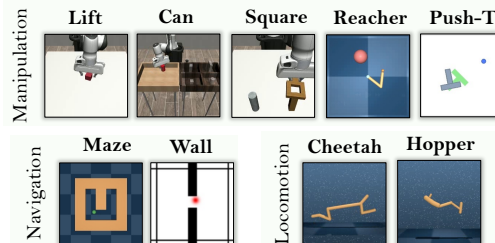


Figure 5: Environments used in Experiments.

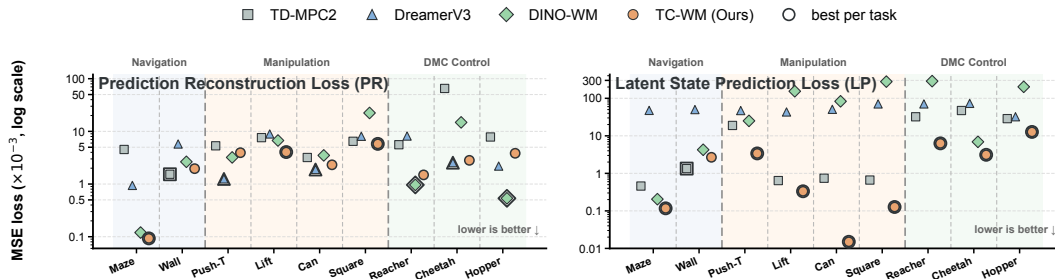


Figure 6: World model prediction accuracy. We report Prediction Reconstruction Loss (PR) and Latent State Prediction Loss (LP) (lower is better) on offline datasets over 300k training steps.

**Evaluation.** We evaluate prediction quality using image-space reconstruction, latent rollout error, and SSIM. For goal-reaching tasks, we report success rate (SR); for DMC locomotion tasks, we report episode return.

**Choices of Visual Foundation Models.** We use DINOv2 [Oquab et al., 2023] as the default frozen visual encoder, matching DINO-WM for fair comparison. Figure 9 additionally evaluates DINOv3 [Siméoni et al., 2025] and Cosmos [Agarwal et al., 2025] as alternative visual foundation models; implementation details are in Appendix A.2.

**Baselines.** We compare against four representative world-model baselines. **TD-MPC2** [Hansen et al., 2024] learns compact latent dynamics for model-predictive control, adapted here to replay-only offline training. **DreamerV3** [Hafner et al., 2025] learns a recurrent latent generative world model with image reconstruction and imagination. **MuZero** [Schrittwieser et al., 2020], a representative task-oriented latent-dynamics method, is reproduced inside our framework as a representation/dynamics trained on the same offline trajectories (Section A.4). **DINO-WM** [Zhou et al., 2025] predicts future frozen DINO embeddings directly and is the closest embedding-space baseline. All methods use the same offline trajectories of images, actions, and proprioception.

### 3.2 Results and Analysis

**World Model Prediction.** Figure 6 separates image reconstruction from latent rollout accuracy. Image-space error is task-dependent: TC-WM is competitive on Lift, Square, and Maze, while baselines perform better on visually complex tasks like Push-T, Cheetah, and Hopper. In contrast, TC-WM achieves the lowest latent prediction error on nearly all tasks, especially in manipulation settings where accurate dynamics are crucial. This suggests that compressing frozen visual embeddings preserves key structure while yielding a more stable state space.

Open-loop rollouts in Figure 7 provide the qualitative counterpart: TC-WM better preserves contact events, gripper motion, and object placement over long horizons. The main tradeoff is image-space fidelity on visually complex dynamics, where compact projection can discard low-level details.

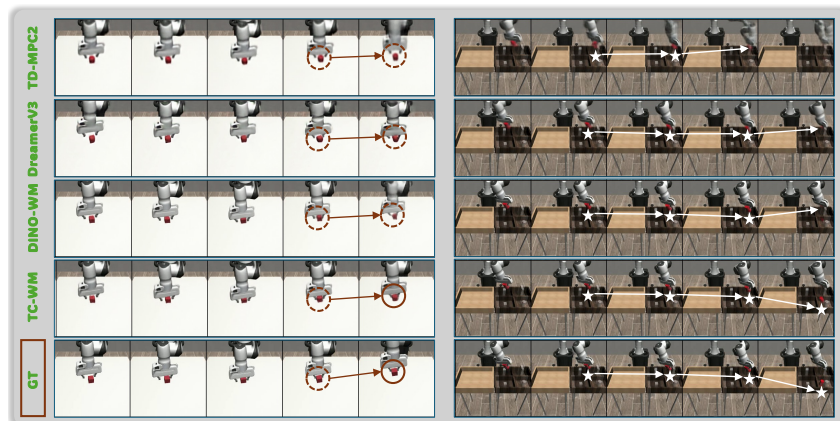


Figure 7: Open-loop rollouts on RoboMimic: Lift (left half) and Can (right half).

**Planning Performance.** Figure 8 evaluates planning with CEM for low-dimensional control and LDP [Xie et al., 2025] for high-dimensional manipulation. TC-WM is competitive across CEM tasks and obtains the clearest gains under LDP on Lift, Can, and Square, where planning depends on precise long-horizon object interaction. This supports the main empirical claim: task-centric latents matter most when the action space is complex and control-relevant physical state must remain stable.

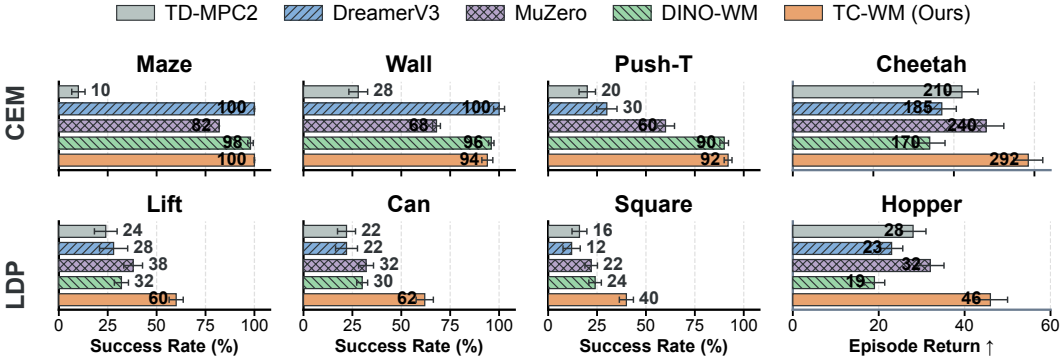


Figure 8: Planning performance of TC-WM against TD-MPC2, DreamerV3, MuZero, and DINO-WM. (Top) CEM planning on Maze, Wall, Push-T (success rate, %) and on Cheetah and Hopper (episode return; the rightmost column has a blue-grey background to flag the change of metric). (Bottom) LDP planning on Lift, Can, and Square, where high-dimensional action spaces make task-centric latent dynamics especially important. TC-WM matches the strongest baseline on the saturated CEM tasks and is the only method that surpasses DINO-WM on every LDP task.

**Architecture and Module Ablations.** Figure 9 summarizes architecture-level ablations on RoboMimic. Random projection performs poorly, showing that dimensionality reduction alone is not enough. DINOv2 and DINOv3 provide the strongest foundation features, while Cosmos is weaker in this setting. Among projection heads, the linear map gives the best balance between planning success and embedding reconstruction.

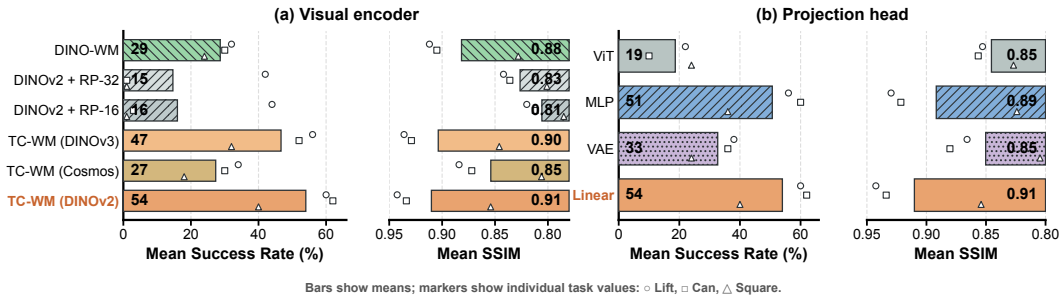


Figure 9: Architecture/module ablations on RoboMimic. (a) Visual encoder or latent-source choice and (b) projection-head ablation, each showing success rate on the left and mirrored SSIM on the right. RP denotes randomly projected DINOv2 embeddings. Bars show means over Lift, Can, and Square; markers show individual task values.

**Robustness to unseen visual perturbations.** Following the test-time perturbation protocol of DINO-WM [Zhou et al., 2025], we feed each frozen world model inputs corrupted by *Gaussian noise* ( $\sigma=0.1$ ) or *color jitter* (per-channel scale  $\in [0.8, 1.2]$ , shift  $\sigma=0.05$ ). Figure 10 shows TC-WM recovers the manipulator and object pose under both perturbations, and its relative SSIM drop is consistently smaller than DINO-WM’s, e.g.,  $-2.5\%$  vs.  $-4.8\%$  under noise on Lift.

### 3.3 Evaluation on Learned Representations

**Linear Probing on Latent Representation.** To validate that TC-WM learns task-centric representations, we probe the learned latent space using ground-truth *full* states, including proprioceptive signals, object states, and goal-related indicators. We use the same protocol for all methods: train a linear regressor from each method’s latent to the target state variables and report  $R^2$  scores. The

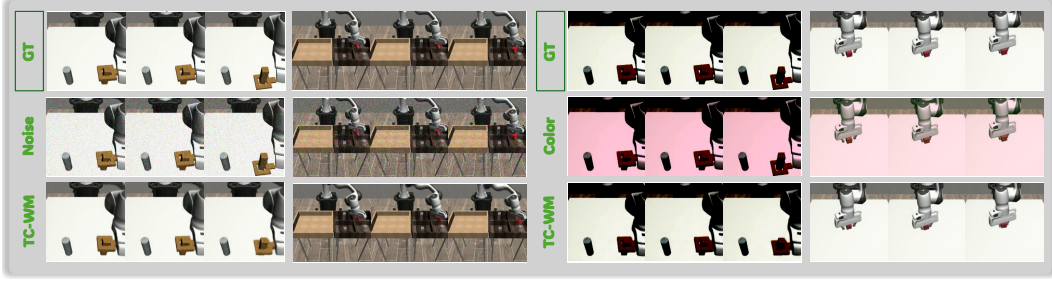


Figure 10: Rollouts under unseen visual perturbations. *Left*: Gaussian noise on Square and Can. *Right*: color jitter on Can and Lift.

linear-probing panels in Figure 2 show that TC-WM more accurately recovers these task-centric variables, indicating that its latent space is not merely predictive but physically grounded.

**Projection Design Rationale.** Figure 9 also explains why we use a linear projection. Frozen visual embeddings already contain structured semantic directions, so the projection mainly needs to select and align a compact task-centric subspace rather than relearn visual abstraction. More complex projectors can distort this geometry or introduce optimization and bottleneck effects. This empirical trend is consistent with Theorem 1, which shows that a linear transformation is sufficient to recover the task-centric subspace up to an affine mapping.

**Ablation on Loss Components.** Figure 11 isolates the role of each loss on Lift. Removing embedding reconstruction causes the largest collapse, reducing both planning success and SSIM, which confirms that  $\mathcal{L}_{\text{rec}}$  anchors the compact latent to the foundation embedding space. Removing proprioceptive supervision mostly preserves SSIM but lowers SR, showing that alignment shapes the latent for control rather than visual fidelity. The  $z^s/z^c$  split dimension has only a modest effect, suggesting that performance is not sensitive to this hyperparameter.

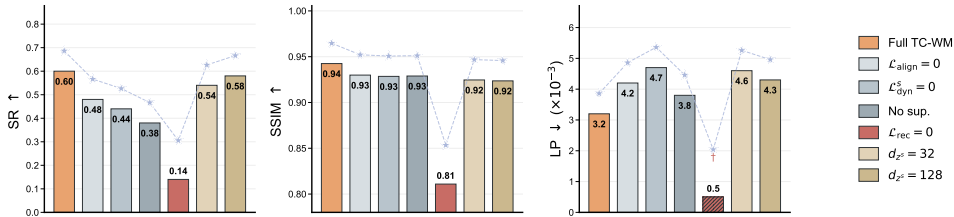


Figure 11: Ablation on loss components and latent split dimension (Lift, 100 epochs).  $\mathcal{L}_{\text{rec}}=0$  collapses both planning (SR) and visual fidelity (SSIM); proprioceptive supervision ( $\mathcal{L}_{\text{align}}$ ,  $\mathcal{L}_{\text{dyn}}^s$ ) is essential for planning;  $z^s$  split dimension has modest effect. † Without embedding reconstruction, the latent collapses and trivially predicts itself, so LP is artificially low.

## 4 Conclusion

In this paper, we propose TC-WM, a task-sufficient world modeling framework that abstracts visual foundation embeddings into compact, task-centric latent spaces for accurate world modeling, planning, and control. By learning dynamics in this latent space rather than directly in high-dimensional embeddings, TC-WM improves predictive accuracy and planning performance in reward-free offline settings. Our results highlight the importance of projecting visual foundation embeddings into a task-centric subspace for world modeling and effective control, rather than using them verbatim.

**Limitations and Future Work.** TC-WM requires a training-time signal that exposes physical information (here proprioception  $s_t^p$ ); when unavailable, distilled physical proxies or multi-view supervision are natural substitutes. Two follow-up directions we find promising are using TC-WM as a lightweight downstream-alignment module on top of a larger pretrained generative world model, and training a generative dynamics model directly on the foundation embedding space to combine pixel-free supervision with control-centric structure. Details are in Section E.

## References

- Niket Agarwal, Arslan Ali, Maciej Bala, Yogesh Balaji, Erik Barker, Tiffany Cai, Prithvijit Chattopadhyay, Yongxin Chen, Yin Cui, Yifan Ding, et al. Cosmos world foundation model platform for physical ai. *arXiv preprint arXiv:2501.03575*, 2025.
- Eloi Alonso, Adam Jelley, Vincent Micheli, Anssi Kanervisto, Amos J Storkey, Tim Pearce, and François Fleuret. Diffusion for world modeling: Visual details matter in atari. *Advances in Neural Information Processing Systems*, 37:58757–58791, 2024.
- Mahmoud Assran, Quentin Duval, Ishan Misra, Piotr Bojanowski, Pascal Vincent, Michael Rabbat, Yann LeCun, and Nicolas Ballas. Self-supervised learning from images with a joint-embedding predictive architecture. In *Proceedings of the IEEE/CVF Conference on Computer Vision and Pattern Recognition*, pages 15619–15629, 2023.
- Mido Assran, Adrien Bardes, David Fan, Quentin Garrido, Russell Howes, Matthew Muckley, Ammar Rizvi, Claire Roberts, Koustuv Sinha, Artem Zholus, et al. V-jepa 2: Self-supervised video models enable understanding, prediction and planning. *arXiv preprint arXiv:2506.09985*, 2025.
- Alessandro Astolfi. Model reduction by moment matching for linear and nonlinear systems. *IEEE Transactions on Automatic Control*, 55(10):2321–2336, 2010.
- Federico Baldassarre, Marc Szafraniec, Basile Terver, Vasil Khalidov, Francisco Massa, Yann LeCun, Patrick Labatut, Maximilian Seitzer, and Piotr Bojanowski. Back to the features: Dino as a foundation for video world models. *arXiv preprint arXiv:2507.19468*, 2025.
- Adrien Bardes, Jean Ponce, and Yann LeCun. Vicreg: Variance-invariance-covariance regularization for self-supervised learning. *arXiv preprint arXiv:2105.04906*, 2021.
- Adrien Bardes, Quentin Garrido, Jean Ponce, Xinlei Chen, Michael Rabbat, Yann LeCun, Mahmoud Assran, and Nicolas Ballas. Revisiting feature prediction for learning visual representations from video. *arXiv preprint arXiv:2404.08471*, 2024.
- Andreas Blattmann, Robin Rombach, Huan Ling, Tim Dockhorn, Seung Wook Kim, Sanja Fidler, and Karsten Kreis. Align your latents: High-resolution video synthesis with latent diffusion models. In *Proceedings of the IEEE/CVF conference on computer vision and pattern recognition*, pages 22563–22575, 2023.
- Ting Chen, Simon Kornblith, Mohammad Norouzi, and Geoffrey Hinton. A simple framework for contrastive learning of visual representations. In *International conference on machine learning*, pages 1597–1607. PmLR, 2020.
- Cheng Chi, Zhenjia Xu, Siyuan Feng, Eric Cousineau, Yilun Du, Benjamin Burchfiel, Russ Tedrake, and Shuran Song. Diffusion policy: Visuomotor policy learning via action diffusion. *The International Journal of Robotics Research*, 44(10-11):1684–1704, 2025.
- Alexey Dosovitskiy. An image is worth 16x16 words: Transformers for image recognition at scale. *arXiv preprint arXiv:2010.11929*, 2020.
- Andreas Draeger, Sebastian Engell, and Horst Ranke. Model predictive control using neural networks. *IEEE Control Systems Magazine*, 15(5):61–66, 1995.
- Fan Feng, Selena Ge, Minghao Fu, Zijian Li, Yujia Zheng, Zeyu Tang, Yingyao Hu, Biwei Huang, and Kun Zhang. Ada-diffuser: Latent-aware adaptive diffusion for decision-making. In *The Fourteenth International Conference on Learning Representations*, 2026.
- Chelsea Finn and Sergey Levine. Deep visual foresight for planning robot motion. In *2017 IEEE international conference on robotics and automation (ICRA)*, pages 2786–2793. IEEE, 2017.
- Justin Fu, Aviral Kumar, Ofir Nachum, George Tucker, and Sergey Levine. D4rl: Datasets for deep data-driven reinforcement learning. *arXiv preprint arXiv:2004.07219*, 2020.

- Klaus Greff, Raphaël Lopez Kaufman, Rishabh Kabra, Nick Watters, Christopher Burgess, Daniel Zoran, Loic Matthey, Matthew Botvinick, and Alexander Lerchner. Multi-object representation learning with iterative variational inference. In *International conference on machine learning*, pages 2424–2433. PMLR, 2019.
- Jean-Bastien Grill, Florian Strub, Florent Alché, Corentin Tallec, Pierre Richemond, Elena Buchatskaya, Carl Doersch, Bernardo Avila Pires, Zhaohan Guo, Mohammad Gheshlaghi Azar, et al. Bootstrap your own latent—a new approach to self-supervised learning. *Advances in neural information processing systems*, 33:21271–21284, 2020.
- David Ha and Jürgen Schmidhuber. World models. *arXiv preprint arXiv:1803.10122*, 2(3):440, 2018.
- Tuomas Haarnoja, Aurick Zhou, Pieter Abbeel, and Sergey Levine. Soft actor-critic: Off-policy maximum entropy deep reinforcement learning with a stochastic actor. In *International conference on machine learning*, pages 1861–1870. Pmlr, 2018.
- Danijar Hafner, Timothy Lillicrap, Jimmy Ba, and Mohammad Norouzi. Dream to control: Learning behaviors by latent imagination. In *International Conference on Learning Representations*, 2020. URL <https://openreview.net/forum?id=S1l0TC4tDS>.
- Danijar Hafner, Timothy P Lillicrap, Mohammad Norouzi, and Jimmy Ba. Mastering atari with discrete world models. In *International Conference on Learning Representations*, 2021. URL <https://openreview.net/forum?id=0oabwyZb0u>.
- Danijar Hafner, Jurgis Pasukonis, Jimmy Ba, and Timothy Lillicrap. Mastering diverse domains through world models. *arXiv preprint arXiv:2301.04104*, 2023.
- Danijar Hafner, Jurgis Pasukonis, Jimmy Ba, and Timothy Lillicrap. Mastering diverse control tasks through world models. *Nature*, pages 1–7, 2025.
- N Hansen, X Wang, and H Su. Temporal difference learning for model predictive control. In *International Conference on Machine Learning, PMLR*, 2022.
- Nicklas Hansen, Hao Su, and Xiaolong Wang. TD-MPC2: Scalable, robust world models for continuous control. In *The Twelfth International Conference on Learning Representations*, 2024. URL <https://openreview.net/forum?id=0xh5CstDJU>.
- Nicklas Hansen, Hao Su, and Xiaolong Wang. Learning massively multitask world models for continuous control. *arXiv preprint arXiv:2511.19584*, 2025.
- Mark K Ho, David Abel, Carlos G Correa, Michael L Littman, Jonathan D Cohen, and Thomas L Griffiths. People construct simplified mental representations to plan. *Nature*, 606(7912):129–136, 2022.
- Yafei Hu, Quanting Xie, Vidhi Jain, Jonathan Francis, Jay Patrikar, Nikhil Keetha, Seungchan Kim, Yaqi Xie, Tianyi Zhang, Hao-Shu Fang, et al. Toward general-purpose robots via foundation models: A survey and meta-analysis. *arXiv preprint arXiv:2312.08782*, 2023.
- Leslie Pack Kaelbling, Michael L Littman, and Anthony R Cassandra. Planning and acting in partially observable stochastic domains. *Artificial intelligence*, 101(1-2):99–134, 1998.
- Ilyes Khemakhem, Diederik Kingma, Ricardo Monti, and Aapo Hyvarinen. Variational autoencoders and nonlinear ica: A unifying framework. In *International conference on artificial intelligence and statistics*, pages 2207–2217. PMLR, 2020.
- Timothée Lesort, Natalia Díaz-Rodríguez, Jean-François Goudou, and David Filliat. State representation learning for control: An overview. *Neural Networks*, 108:379–392, 2018.
- Haotian Liu, Chunyuan Li, Qingyang Wu, and Yong Jae Lee. Visual instruction tuning. *Advances in neural information processing systems*, 36:34892–34916, 2023.
- Francesco Locatello, Dirk Weissenborn, Thomas Unterthiner, Aravindh Mahendran, Georg Heigold, Jakob Uszkoreit, Alexey Dosovitskiy, and Thomas Kipf. Object-centric learning with slot attention. *Advances in neural information processing systems*, 33:11525–11538, 2020.

- Ajay Mandlekar, Yuke Zhu, Animesh Garg, Jonathan Booher, Max Spero, Albert Tung, Julian Gao, John Emmons, Ankur Gupta, Silvio Savarese, and Li Fei-Fei. RoboTurk: A crowdsourcing platform for robotic skill learning through imitation. In *Conference on Robot Learning*, pages 610–629, 2018.
- Ajay Mandlekar, Danfei Xu, Josiah Wong, Soroush Nasiriany, Chen Wang, Rohun Kulkarni, Li Fei-Fei, Silvio Savarese, Yuke Zhu, and Roberto Martín-Martín. What matters in learning from offline human demonstrations for robot manipulation. *arXiv preprint arXiv:2108.03298*, 2021.
- Francesca Mastrogioseppe and Srdjan Ostojic. Linking connectivity, dynamics, and computations in low-rank recurrent neural networks. *Neuron*, 99(3):609–623, 2018.
- Aran Nayebi, Rishi Rajalingham, Mehrdad Jazayeri, and Guangyu Robert Yang. Neural foundations of mental simulation: Future prediction of latent representations on dynamic scenes. *Advances in Neural Information Processing Systems*, 36:70548–70561, 2023.
- Aaron van den Oord, Yazhe Li, and Oriol Vinyals. Representation learning with contrastive predictive coding. *arXiv preprint arXiv:1807.03748*, 2018.
- Maxime Oquab, Timothée Darcet, Théo Moutakanni, Huy Vo, Marc Szafraniec, Vasil Khalidov, Pierre Fernandez, Daniel Haziza, Francisco Massa, Alaaeldin El-Nouby, et al. Dinov2: Learning robust visual features without supervision. *arXiv preprint arXiv:2304.07193*, 2023.
- Deepak Pathak, Pulkit Agrawal, Alexei A Efros, and Trevor Darrell. Curiosity-driven exploration by self-supervised prediction. In *International conference on machine learning*, pages 2778–2787. PMLR, 2017.
- Deepak Pathak, Parsa Mahmoudieh, Guanghao Luo, Pulkit Agrawal, Dian Chen, Yide Shentu, Evan Shelhamer, Jitendra Malik, Alexei A Efros, and Trevor Darrell. Zero-shot visual imitation. In *Proceedings of the IEEE conference on computer vision and pattern recognition workshops*, pages 2050–2053, 2018.
- William Peebles and Saining Xie. Scalable diffusion models with transformers. In *Proceedings of the IEEE/CVF international conference on computer vision*, pages 4195–4205, 2023.
- Alec Radford, Jong Wook Kim, Chris Hallacy, Aditya Ramesh, Gabriel Goh, Sandhini Agarwal, Girish Sastry, Amanda Askell, Pamela Mishkin, Jack Clark, et al. Learning transferable visual models from natural language supervision. In *International conference on machine learning*, pages 8748–8763. PmLR, 2021.
- Rishi Rajalingham, Aida Piccato, and Mehrdad Jazayeri. Recurrent neural networks with explicit representation of dynamic latent variables can mimic behavioral patterns in a physical inference task. *Nature Communications*, 13(1):5865, 2022.
- Geoffrey Roeder, Luke Metz, and Durk Kingma. On linear identifiability of learned representations. In *International Conference on Machine Learning*, pages 9030–9039. PMLR, 2021.
- Moritz Schneider, Robert Krug, Narunas Vaskevicius, Luigi Palmieri, and Joschka Boedecker. The surprising ineffectiveness of pre-trained visual representations for model-based reinforcement learning. *Advances in Neural Information Processing Systems*, 37:32916–32946, 2024.
- Bernhard Schölkopf, Francesco Locatello, Stefan Bauer, Nan Rosemary Ke, Nal Kalchbrenner, Anirudh Goyal, and Yoshua Bengio. Toward causal representation learning. *Proceedings of the IEEE*, 109(5):612–634, 2021.
- Julian Schrittwieser, Ioannis Antonoglou, Thomas Hubert, Karen Simonyan, Laurent Sifre, Simon Schmitt, Arthur Guez, Edward Lockhart, Demis Hassabis, Thore Graepel, et al. Mastering atari, go, chess and shogi by planning with a learned model. *Nature*, 588(7839):604–609, 2020.
- Ramanan Sekar, Oleh Rybkin, Kostas Daniilidis, Pieter Abbeel, Danijar Hafner, and Deepak Pathak. Planning to explore via self-supervised world models. In *International conference on machine learning*, pages 8583–8592. PMLR, 2020.

- Oriane Siméoni, Huy V Vo, Maximilian Seitzer, Federico Baldassarre, Maxime Oquab, Cijo Jose, Vasil Khalidov, Marc Szafraniec, Seungeun Yi, Michaël Ramamonjisoa, et al. Dinov3. *arXiv preprint arXiv:2508.10104*, 2025.
- Richard S Sutton. Integrated architectures for learning, planning, and reacting based on approximating dynamic programming. In *Machine learning proceedings 1990*, pages 216–224. Elsevier, 1990.
- Richard S Sutton. Dyna, an integrated architecture for learning, planning, and reacting. *ACM Sigart Bulletin*, 2(4):160–163, 1991.
- Jinzhou Tang, Fan Feng, Minghao Fu, Wenjun Lin, Biwei Huang, and Keze Wang. Dreamsac: Learning hamiltonian world models via symmetry exploration. *arXiv preprint arXiv:2603.07545*, 2026.
- Yuval Tassa, Yotam Doron, Alistair Muldal, Tom Erez, Yazhe Li, Diego de Las Casas, David Budden, Abbas Abdolmaleki, Josh Merel, Andrew Lefrancq, et al. Deepmind control suite. *arXiv preprint arXiv:1801.00690*, 2018.
- Manuel Watter, Jost Springenberg, Joschka Boedecker, and Martin Riedmiller. Embed to control: A locally linear latent dynamics model for control from raw images. *Advances in neural information processing systems*, 28, 2015.
- Grady Williams, Paul Drews, Brian Goldfain, James M Rehg, and Evangelos A Theodorou. Information-theoretic model predictive control: Theory and applications to autonomous driving. *IEEE Transactions on Robotics*, 34(6):1603–1622, 2018.
- Yilin Wu, Anqi Li, Tucker Hermans, Fabio Ramos, Andrea Bajcsy, and Claudia Pérez-D’Arpino. Do what you say: Steering vision-language-action models via runtime reasoning-action alignment verification. *arXiv preprint arXiv:2510.16281*, 2025.
- Amber Xie, Oleh Rybkin, Dorsa Sadigh, and Chelsea Finn. Latent diffusion planning for imitation learning. *arXiv preprint arXiv:2504.16925*, 2025.
- Sihyun Yu, Sangkyung Kwak, Huiwon Jang, Jongheon Jeong, Jonathan Huang, Jinwoo Shin, and Saining Xie. Representation alignment for generation: Training diffusion transformers is easier than you think. In *International Conference on Learning Representations*, 2025.
- Jiahao Zhang, Muqing Jiang, Nanru Dai, Taiming Lu, Arda Uzunoglu, Shunchi Zhang, Yana Wei, Jiahao Wang, Vishal M Patel, Paul Pu Liang, et al. World-in-world: World models in a closed-loop world. *arXiv preprint arXiv:2510.18135*, 2025.
- Boyang Zheng, Nanye Ma, Shengbang Tong, and Saining Xie. Diffusion transformers with representation autoencoders. *arXiv preprint arXiv:2510.11690*, 2025.
- Gaoyue Zhou, Hengkai Pan, Yann LeCun, and Lerrel Pinto. DINO-WM: World models on pre-trained visual features enable zero-shot planning. In *Forty-second International Conference on Machine Learning*, 2025. URL <https://openreview.net/forum?id=D5RNACOZEI>.
- Yuke Zhu, Josiah Wong, Ajay Mandlekar, Roberto Martín-Martín, Abhishek Joshi, Soroush Nasiriany, and Yifeng Zhu. robosuite: A modular simulation framework and benchmark for robot learning. *arXiv preprint arXiv:2009.12293*, 2020.
- Roland S Zimmermann, Yash Sharma, Steffen Schneider, Matthias Bethge, and Wieland Brendel. Contrastive learning inverts the data generating process. In *International conference on machine learning*, pages 12979–12990. PMLR, 2021.

---

***Appendix of “Back to Parsimonious Latents:  
Learning Task-Centric World Models from Visual  
Foundations”***

---

<b>A</b>	<b>Experiment Details</b>	<b>15</b>
A.1	Environments and Dataset Collection . . . . .	15
A.2	Details of Selected Visual Foundation Models . . . . .	15
A.3	Pipeline of Planning on Manipulation Tasks . . . . .	16
A.4	Implementation Details of Baselines . . . . .	17
A.5	Compute Resources . . . . .	17
<b>B</b>	<b>Theoretical Rationale: When and How can We Learn Task-centric Representation from Visual Foundations?</b>	<b>18</b>
B.1	Illustration and Analysis . . . . .	18
B.2	Proof of Theorem A1 . . . . .	21
<b>C</b>	<b>More Visualizations and Analysis</b>	<b>26</b>
<b>D</b>	<b>Extended Related Work</b>	<b>28</b>
<b>E</b>	<b>Limitations and Future Work</b>	<b>31</b>

---

## A Experiment Details

### A.1 Environments and Dataset Collection

We evaluate across nine environments. Below we describe the data source for each group, organized by collection method.

**DINO-WM released data** (Maze, Wall, Push-T). We directly adopt the released datasets from DINO-WM [Zhou et al., 2025]. Maze follows the PointMaze environment of D4RL [Fu et al., 2020], where a force-actuated 2-DoF ball navigates to a goal; the dataset contains 2000 random trajectories. Wall is a 2D room-to-room navigation task with 1920 fixed-wall and 10240 randomized-wall trajectories. Push-T, adapted from Chi et al. [2025], uses 18.5k expert demonstrations and 20k randomized trajectories for a block-pushing task.

**RoboMimic official demonstrations** (Lift, Can, Square). We use the official demonstration datasets released by the RoboMimic benchmark [Mandlekar et al., 2021]. All three tasks are simulated in robosuite [Zhu et al., 2020] with MuJoCo, using a 7-DoF Franka Panda robot. Demonstrations are collected via the RoboTurk teleoperation platform [Mandlekar et al., 2018], where human operators control the robot arm through a smartphone interface. We use the Proficient-Human (PH) demonstrations, which are collected by a single skilled operator: 200 trajectories each for Lift (robosuite Lift), Can (PickPlaceCan), and Square (NutAssemblySquare). Image observations are rendered from two simulated cameras (a front-facing agentview and a wrist-mounted robot0\_eye\_in\_hand).

**TD-MPC2 rollouts** (Reacher, Cheetah, Hopper). We generate offline trajectories by rolling out pretrained TD-MPC2 checkpoints from Hansen et al. [2025] in the DeepMind Control Suite. For each task we collect trajectories over multiple rounds, with actions produced by the TD-MPC2 policy conditioned on the current observation. We record rendered frames and low-dimensional state observations at each step. To ensure demonstration quality we apply a return-based filter: episodes are accepted only if their total return exceeds  $0.75 \times \text{median}$  (or  $1.25 \times \text{median}$  when negative).

Table A1: Action and proprioception dimensionalities of all nine evaluation environments. The Robomimic manipulation tasks (Lift, Can, Square) have markedly higher-dimensional action and proprioceptive spaces than the navigation and DMC continuous-control benchmarks, justifying our use of LDP and our claim that they form the most challenging planning regime in this study.

Category	Dataset	Action dim	Proprio dim	Action type	Planner
Navigation	Maze	2	4	continuous force $(F_x, F_y)$	CEM
	Wall	2	4	continuous velocity $(v_x, v_y)$	CEM
Pushing	Push-T	2	5	continuous 2D target $(t_x, t_y)$	CEM
Manipulation	Lift	7	43	6 DoF joint velocity + gripper	LDP
	Can	7	43	6 DoF joint velocity + gripper	LDP
	Square	7	43	6 DoF joint velocity + gripper	LDP
DMC control	Reacher	2	6	continuous joint torque	CEM
	Cheetah	6	17	continuous joint torque	CEM
	Hopper	4	15	continuous joint torque	CEM

### A.2 Details of Selected Visual Foundation Models

**DINOv2.** We use the TorchHub implementation from facebookresearch/dinov2 with backbone dinov2\_vits14. Given an input image tensor  $x \in \mathbb{R}^{B \times 3 \times H \times W}$ , we extract patch-level features as the representation. This yields a sequence of normalized patch tokens of shape  $(B, N, D)$ , where  $D = \text{num\_features}$  (384 for ViT-S/14) and  $N = (H/\text{patch\_size}) \cdot (W/\text{patch\_size})$  with  $\text{patch\_size} = 14$ , matching the configuration used by DINO-WM [Zhou et al., 2025].

**DINOv3.** We use the version facebook/dinov3-vitb16-pretrain-lvd1689m. The encoder takes RGB images  $x \in \mathbb{R}^{B \times 3 \times H \times W}$  as input, which are normalized using the model-provided mean and standard deviation when available (otherwise ImageNet statistics). DINOv3 employs a

ViT-B/16 backbone with patch size  $16 \times 16$  and hidden dimension  $D = 768$ . The raw output has shape  $(B, 1+R+N, D)$ , where  $N = (H/16) \cdot (W/16)$  denotes the number of patch tokens and  $R$  the number of register tokens. Following standard practice, we discard the CLS token and any register tokens, retaining only the patch tokens of the shape  $\mathbb{R}^{B \times N \times 768}$  as the final visual representation.

**Cosmos CI Tokenizer.** For Cosmos, we use the NVIDIA/Cosmos-0.1-Tokenizer-CI8x8 tokenizer encoder loaded from a TorchScript checkpoint. Images are resized to  $112 \times 112$  and encoded in FP16. The encoder produces latents of shape  $(B, C, H', W')$  (with  $C = 16$  in our setting), which we reshape into tokens  $(B, H'W', C)$ . With patch size 8 and image size 112, this yields a  $14 \times 14$  token grid (*i.e.*, 196 tokens), aligning with the token-count budget used by the rest of the architecture.

### A.3 Pipeline of Planning on Manipulation Tasks

In this subsection, we describe the latent-space planning and control procedure. Depending on the task setup and data modality, we employ the Cross-Entropy Method (CEM) for navigation tasks and Latent Diffusion Planning (LDP) framework [Xie et al., 2025] for manipulation tasks, based on the complexity of action space.

**On Navigation Tasks.** For low-dimensional action spaces we plan directly with CEM, treating the encoded goal latent as the target state.

- (1) **Latent Encoding.** Given the current observation  $\mathbf{o}_0$  and the goal observation  $\mathbf{o}_g$ , both represented as RGB images, we first extract visual embeddings  $\mathbf{x}_0 = f_{\text{emb}}(\mathbf{o}_0)$  and  $\mathbf{x}_g = f_{\text{emb}}(\mathbf{o}_g)$ , then encode them into latent states:

$$\mathbf{z}_0 = q(\mathbf{z}_0 | \mathbf{x}_0), \quad \mathbf{z}_g = q(\mathbf{z}_g | \mathbf{x}_g).$$

- (2) **Planning Objective.** The objective is to minimize the distance between the predicted final latent  $\hat{\mathbf{z}}_{H_p}$  and the goal latent  $\mathbf{z}_g$ :

$$\mathcal{C} = \|\hat{\mathbf{z}}_{H_p} - \mathbf{z}_g\|^2, \quad \text{where} \quad \hat{\mathbf{z}}_{H_p} = f_{\theta}^{H_p}(\mathbf{z}_0, \mathbf{a}_{0:H_p-1}).$$

- (3) **Action Sampling.** At each planning iteration, CEM samples a population of  $N$  action sequences  $\{\mathbf{a}_{0:H_p-1}^i\}_{i=1}^N$  from a Gaussian distribution. The initial mean and covariance are initialized as  $\boldsymbol{\mu}_0$  and  $\boldsymbol{\Sigma}_0$ .

- (4) **Trajectory Rollout.** For each sampled sequence, the learned world model predicts the latent rollout:

$$\hat{\mathbf{z}}_t = f_{\theta}^t(\mathbf{z}_0, \mathbf{a}_{0:t-1}), \quad t = 1, \dots, H_p,$$

and the trajectory cost  $\mathcal{C}^i$  is computed according to the objective above.

- (5) **Elite Selection and Update.** The top  $K$  trajectories with the lowest costs are selected as elites, and the sampling distribution is updated by:

$$\boldsymbol{\mu} \leftarrow \text{mean}(\mathbf{a}^{(1:K)}), \quad \boldsymbol{\Sigma} \leftarrow \text{cov}(\mathbf{a}^{(1:K)}).$$

- (6) **Iteration.** A new population of  $N$  trajectories is resampled from the updated Gaussian, and the process is repeated for a fixed number of iterations  $T_{\text{cem}}$ .

- (7) **Execution.** After optimization, the first  $H_a$  actions  $\mathbf{a}_{0:H_a-1}$  are executed in the environment. At the next timestep, a new observation  $\mathbf{x}_{H_a}$  is encoded and the planning process repeats, forming a closed-loop receding-horizon controller.

**On Manipulation Tasks.** For high-dimensional, contact-rich actions we couple TC-WM with the Latent Diffusion Planning (LDP) framework [Xie et al., 2025].

- (1) **Input Encoding.** Given the current observation  $\mathbf{o}_0$ , goal observation  $\mathbf{o}_g$ , and proprioceptive state  $\mathbf{s}_0^p$ , we use TC-WM to encode observations into latent states:

$$\mathbf{z}_0 = q(\mathbf{z}_0 | f_{\text{emb}}(\mathbf{o}_0)), \quad \mathbf{z}_g = q(\mathbf{z}_g | f_{\text{emb}}(\mathbf{o}_g)).$$

- (2) **Planning Objective.** The planner forecasts a sequence of future latent states  $[\hat{\mathbf{z}}_{k+1}, \dots, \hat{\mathbf{z}}_{k+H_p}]$  conditioned on  $\mathbf{z}_k$ , optimized by the diffusion loss:

$$\mathcal{L}_{\text{planner}}(\psi) = \mathbb{E}_{t, \epsilon} [\|\epsilon_{\psi}(\hat{\mathbf{z}}_{k+1}, \dots, \hat{\mathbf{z}}_{k+H_p}; \mathbf{z}_k, t) - \epsilon\|^2].$$

(3) **Inverse Dynamics Model.** The IDM reconstructs actions between latent states via:

$$\mathcal{L}_{\text{IDM}}(\xi) = \mathbb{E}_{t,\epsilon} [\|\epsilon_{\xi}(\hat{\mathbf{a}}_k; \mathbf{z}_k, \mathbf{z}_{k+1}, t) - \epsilon\|^2].$$

- (4) **Latent Trajectory Sampling.** At inference, the planner samples  $\hat{\mathbf{z}}_{k+1}, \dots, \hat{\mathbf{z}}_{k+H_p} \sim \mathcal{N}(0, I)$  and iteratively denoises via DDPM updates using  $\epsilon_{\psi}$ .
- (5) **Action Reconstruction.** For each pair  $(\hat{\mathbf{z}}_{k+i}, \hat{\mathbf{z}}_{k+i+1})$ , actions  $\hat{\mathbf{a}}_{k+i}$  are generated through diffusion updates with  $\epsilon_{\xi}$ .
- (6) **Execution and Replanning.** The first  $H_a$  actions  $\hat{\mathbf{a}}_k, \dots, \hat{\mathbf{a}}_{k+H_a-1}$  are executed, and the process repeats with new latent observation  $\mathbf{z}_{k+H_a}$ , forming a closed-loop latent MPC scheme.

#### A.4 Implementation Details of Baselines

**Offline Version of DreamerV3** We implement an offline variant of DreamerV3 [Hafner et al., 2023] that trains exclusively from a fixed replay buffer without any environment interaction. The offline pipeline reads precomputed trajectories (images  $\mathbf{o}_t$ , actions  $\mathbf{a}_t$ , and optional proprio/state and rewards), builds the DreamerV3 replay, and runs the standard DreamerV3 world-model training loop on randomly sampled batches. Evaluation is performed on held-out trajectories by reconstructing and open-loop predicting image sequences: the model encodes a context window of observed frames (posterior) and imagines the future (prior), after which the decoder produces reconstruction/predictions that are compared to ground truth. We keep the original DreamerV3 architecture and losses, and only adapt the data loading, replay ingestion, and offline evaluation logic to accommodate reward-free datasets and dataset-specific observation formats.

**Offline Version of TD-MPC2** We implement TD-MPC2-Offline by adding a replay-only training pipeline to the official TD-MPC2 codebase [Hansen et al., 2024]. The offline trainer removes all environment interaction and learns solely from a fixed dataset. Robomimic demonstrations are loaded from preconverted episode files (RGB video, actions, rewards, terminals), and a fixed replay buffer is built once at startup. Training samples random sequences from this buffer, matching the original TD-MPC2 update equations; no online data is added. For evaluation, we introduce an offline validation split and compute losses on held-out sequences without parameter updates. To align with visual world-model diagnostics, we add a reconstruction decoder and rollout visualization: the decoder is trained with reconstruction loss (with backpropagating into the latent), and rollouts are generated by iterating the latent predictor and decoding predicted latents. Rollout visualization uses the same format as our method. We also extend rollout logic to respect frame skipping by applying the full action sequence within each skip window (rather than subsampling actions), ensuring motion fidelity in long-horizon rollouts.

**Offline Version of MuZero** We adapt MuZero [Schrittwieser et al., 2020] to the offline setting by keeping its three-network decomposition—representation  $h$ , dynamics  $g$ , and prediction  $f$ —and supervising the joint model on fixed trajectories instead of MCTS-driven self-play. In our implementation,  $h$  is the frozen DINOv2 encoder followed by the same compact linear projector as TC-WM,  $g$  is a Transformer next-latent predictor that consumes  $(\mathbf{z}_t, \mathbf{a}_t)$ , and  $f$  collects the per-step heads over the latent. As our datasets carry no dense reward,  $f$  reduces to a policy head  $f_{\xi}^{\pi}$  trained by behaviour cloning on the recorded action; the reward and value heads remain available in the codebase and are deactivated only because the supervision is missing. The training loss is  $\mathcal{L}_{\text{cons}} + 0.25 \|\mathbf{f}_{\xi}^{\pi}(\mathbf{z}_t) - \mathbf{a}_t\|_2^2$ , where  $\mathcal{L}_{\text{cons}}$  matches the unrolled latent to the encoded next-step latent with a stop-gradient on the target, as in the original MuZero. With reward labels the standard  $\mathcal{L}_{\text{cons}} + \mathcal{L}_r + 0.25 \mathcal{L}_v + 0.25 \mathcal{L}_{\pi}$  objective is recovered by simply enabling the reward and Monte-Carlo value heads.

#### A.5 Compute Resources

All training and evaluation runs use a single NVIDIA H100 80 GB GPU per experiment. A typical TC-WM run on `Lift / Can / Square` converges in roughly 8 hours over 100 epochs at peak memory  $\approx 35$  GB; `Push-T / Wall / Maze` converge in 1–2 hours; the DMC tasks (`Reacher`, `Cheetah`, `Hopper`) take 4–6 hours each. Each baseline (TD-MPC2, DreamerV3, MuZero, DINO-WM) uses the same single-H100 budget per environment, with comparable wall-clock times. Aggregating training, evaluation, and the linear-probe / unseen-perturbation studies, the experiments reported in the paper consume roughly 1,200 H100 GPU-hours.

Table A2: Physical interpretation of state observations and their partitioning into three task-centric variable groups for the Robomimic datasets, based on their roles in the robot trajectory. Gray entries are *not* used during training; they serve only as ground-truth references for planning.

Dataset	Proprio	Object	Goal
Lift	robot0_joint_pos, robot0_joint_pos_cos, robot0_eef_pos, robot0_eef_quat_site, robot0_gripper_qvel	robot0_joint_pos_sin, robot0_joint_vel, robot0_eef_quat, robot0_gripper_qpos,	object_pos, object_quat grip_obj_rel_vec
Can	robot0_joint_pos, robot0_joint_pos_cos, robot0_eef_pos, robot0_eef_quat_site, robot0_gripper_qvel	robot0_joint_pos_sin, robot0_joint_vel, robot0_eef_quat, robot0_gripper_qpos,	object_pos, object_quat target_pos, target_quat
Square	robot0_joint_pos, robot0_joint_pos_cos, robot0_eef_pos, robot0_eef_quat_site, robot0_gripper_qvel	robot0_joint_pos_sin, robot0_joint_vel, robot0_eef_quat, robot0_gripper_qpos,	object_pos, object_quat target_pos, target_quat

## B Theoretical Rationale: When and How can We Learn Task-centric Representation from Visual Foundations?

This appendix expands the theoretical statement of Theorem 1. Section B.1 discusses the motivation, the underlying hierarchical generative model, the assumptions, and an empirical sanity check on Lift. Section B.2 contains the full proof.

### B.1 Illustration and Analysis

Understanding when and how task-centric representation can be learned from visual foundation models is critical for modern world-model training. We study this problem through *identifiability*, the asymptotic guarantee of *recovering* a semantically meaningful latent space. The discussion is organized around three previously underexplored questions: (1) how imposing a latent Markov structure on top of visual foundations helps guide world representations; (2) why a simple linear projection is sufficient to transform rich visual features into task-relevant world representations; and (3) empirically validating these claims through ablation studies and linear probing experiments.

We first establish identifiability of task-centric representation in a general framework.

**Definition 2** (Recoverability of Task-Centric Representation). *The estimated  $\hat{\mathbf{z}}_t^s$  is a nontrivial transformation of the true  $\mathbf{z}_t^s$  in the defined process of Sec. 2.2 for each frame.*

We next show that, under mild regularity assumptions, our formulation described in Sec. 2.2 guarantees such recoverability.

**A View from Hierarchical Model.** To justify that learning dynamics from frozen visual embeddings is theoretically sound, we show that the underlying task-centric world representation  $\hat{\mathbf{z}}_t^s$  faithfully captures the physical factors governing the environment. As illustrated in Figure A1, our architecture forms a three-level hierarchy: raw observations  $\mathbf{o}_t$  are mapped to foundation embeddings  $\mathbf{x}_t$  by a frozen encoder, which are then projected into a compact latent  $\mathbf{z}_t = [\mathbf{z}_t^s, \mathbf{z}_t^c]$ . The theorem below guarantees that this hierarchical process preserves the task-relevant factors.

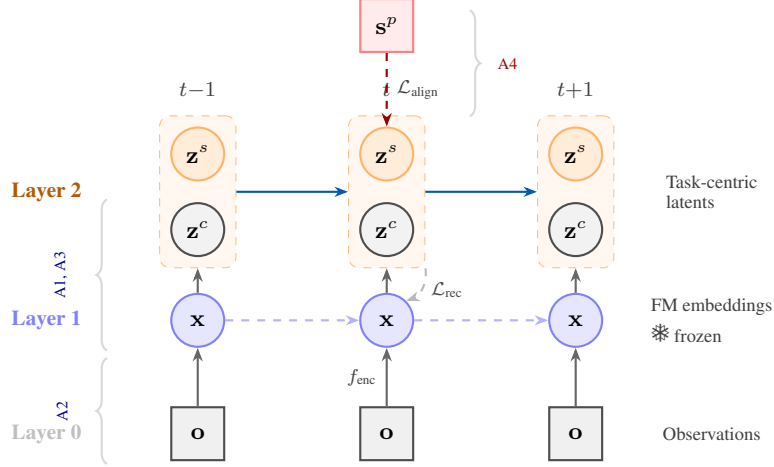


Figure A1: Graphical model of TC-WM’s hierarchical structure. Circles denote latent variables; squares denote observed variables. Observations  $\mathbf{o}_t$  are mapped to frozen FM embeddings  $\mathbf{x}_t$  (Layer 1), then projected to a compact latent  $\mathbf{z}_t = [\mathbf{z}_t^s, \mathbf{z}_t^c]$  (Layer 2, dashed orange box). The unified temporal arrows act on the joint latent  $\mathbf{z}_t$ .  $\mathcal{L}_{\text{align}}$  aligns  $\mathbf{z}_t^s$  with proprioception  $s_t^p$ ;  $\mathcal{L}_{\text{rec}}$  (curved) regularises by reconstructing the embedding from  $\mathbf{z}_t$ . Assumptions A1–A4 of Theorem A1 are annotated.

We first formalize this property through the concept of *recoverability*, which ensures that the learned latents are meaningful transformations of the true task-relevant variables.

### Theorem A1 (Task-centric identifiability from visual embeddings)

Suppose images  $\mathbf{o}_t$ , frozen embeddings  $\mathbf{x}_t$ , and latent variables  $\mathbf{z}_t = [\mathbf{z}_t^s, \mathbf{z}_t^c]$  follow the process in Section 2.2, and the learned latent world model matches the true joint distribution of adjacent embeddings  $\{\mathbf{x}_{t-1}, \mathbf{x}_t, \mathbf{x}_{t+1}\}$ . Assume:

**A1. (Contextual dynamics):**  $L_{\mathbf{x}_{t+1:t+H}|\mathbf{z}_t}$  and  $L_{\mathbf{x}_{t-H:t-1}|\mathbf{x}_{t+1:t+H}}$  are injective and bounded.

**A2. (Latent-observed variability):** For any  $\mathbf{z}_t^{(1)} \neq \mathbf{z}_t^{(2)}$ ,  $p(\mathbf{x}_t | \mathbf{z}_t^{(1)}) \neq p(\mathbf{x}_t | \mathbf{z}_t^{(2)})$ .

**A3. (Differentiability):** There exists a differentiable  $F$  such that  $F[p_{\mathbf{x}_t|\mathbf{z}_t}(\cdot | \mathbf{z}_t)] = h_z(\mathbf{z}_t)$ .

**A4. (Partial alignment):** The alignment objective in Eq. (2) is sufficiently minimized.

Then the learned  $\mathbf{z}_t$  is block-wise identifiable, and the task-centric  $\mathbf{z}_t^s$  is affine-identifiable:

$$\hat{\mathbf{z}}_t = h_z(\mathbf{z}_t), \quad h_z \text{ invertible and } C^1$$

**Latent Space Recovery:** the compact latent preserves the true world state up to reparameterization

$$\mathbf{z}_t^s = \mathbf{A}\hat{\mathbf{z}}_t^s + \mathbf{b}$$

**Task-centric recovery:** the aligned block recovers physical factors up to an affine map

### Takeaway

This theorem justifies our hierarchical paradigm: even though TC-WM learns dynamics in the foundation-embedding space  $\mathbf{x}_t$  rather than in raw pixels  $\mathbf{o}_t$ , the reconstruction and alignment objectives suffice to recover the physically meaningful latent factors that drive the environment. The result connects our approach to a broader family of “dynamics on pretrained encoders,” including recent generative and latent diffusion frameworks such as VideoLDM [Blattmann et al., 2023], DiT [Peebles and Xie, 2023], RAW [Zheng et al., 2025], and REPA [Yu et al., 2025].

**Proof Sketch.** Our argument unfolds in three steps. (1) Under nonparametric assumptions, embeddings  $\mathbf{x}_t$  are invertible transformations of images  $\mathbf{o}_t$  (e.g., DINO or  $\beta$ -VAE), thus preserving the environment’s essential factors. (2) For the embedding-level latent  $\mathbf{z}_t$ , we construct an integral operator over  $2H+1$  adjacent observations and show, via Markov conditional independence and a spectral decomposition argument, that any model matching the true joint distribution of  $\{\mathbf{x}_{t-H:t+H}\}$  recovers  $\mathbf{z}_t$  up to an invertible reparametrisation  $h_z$ . (3) For the task-centric subspace  $\mathbf{z}_t^s$ , the InfoNCE alignment with the proprioception  $\mathbf{s}_t^p$  collapses  $h_z$  on the  $\mathbf{z}^s$ -block to a map that depends only on  $\mathbf{z}_t^s$ , and an exponential-family/dot-product argument then forces it to be affine. The full proof is given below.

**Empirical Verification of Assumptions on Lift.** We complement the theory with direct empirical checks of A1–A4 on a fully trained TC-WM checkpoint (Lift,  $d_z = 256$ ,  $d_s = 64$ ). All probes operate on the patch-mean-pooled latent  $\mathbf{z}_t$  and the mean-pooled foundation embedding  $\mathbf{x}_t$ ; all randomness uses fixed seeds.

**A1 (Contextual Dynamics).** A1 demands that  $L_{\mathbf{x}_{t+1:t+H}|\mathbf{z}_t}$  be both bounded and injective. We probe the closely related forward sensitivity  $\|\Delta\mathbf{x}\|/\|\Delta\mathbf{z}\|$  on 4096 random pairs of (latent, embedding) co-drawn from validation trajectories. The ratio is tightly concentrated, with median 14.37, 5th percentile 11.16, and 95th percentile 19.26 (Figure A2); the lower tail is bounded away from zero, evidencing injectivity, and the upper tail is bounded, evidencing the operator-norm part of A1.

**A2 (Latent-Observed Variability).** A2 demands that distinct latents yield distinct conditional embeddings,  $\mathbf{z}_t^{(1)} \neq \mathbf{z}_t^{(2)} \Rightarrow p(\mathbf{x}_t | \mathbf{z}_t^{(1)}) \neq p(\mathbf{x}_t | \mathbf{z}_t^{(2)})$ . As a population-level surrogate we measure how strongly latent distance predicts embedding distance: Figure A2 plots  $\|\mathbf{z}_i - \mathbf{z}_j\|$  against  $\|\mathbf{x}_i - \mathbf{x}_j\|$  over 2037 random validation pairs. The two distance series are nearly comonotone, with Spearman  $\rho = 0.910$  and Pearson  $\rho = 0.911$ ; in particular, no points cluster near the  $\Delta\mathbf{x} \approx 0$  axis at non-zero  $\Delta\mathbf{z}$ , ruling out the failure mode that A2 forbids.

**A3 (Differentiability).** A3 is satisfied by construction: the projector and embedding decoder are smooth  $C^1$  neural networks, the conditional density  $p(\mathbf{x}_t | \mathbf{z}_t)$  is the output of a differentiable Gaussian decoder, and the functional  $F$  of A3 can be taken as a moment-matching label, which is differentiable in  $\mathbf{z}_t$  via the implicit function theorem. No further empirical check is needed.

**A4 (Partial Alignment).** A4 demands that the InfoNCE alignment loss be sufficiently minimized. We linearly probe both subspaces against the proprioceptive state  $\mathbf{s}_t^p$  (Figure A2). On the full TC-WM checkpoint the task-centric block achieves  $R^2(\hat{\mathbf{z}}_t^s \rightarrow \mathbf{s}_t^p) = 0.592 \pm 0.007$ , a +5.8 absolute-point improvement over the alignment-free ablation ( $0.534 \pm 0.027$ ). The complementary block  $\hat{\mathbf{z}}_t^c$  predicts  $\mathbf{s}_t^p$  at  $R^2 = 0.680 \pm 0.008$ , but its dimensionality is three times higher ( $d_c = 192$  vs  $d_s = 64$ ); on a per-dimension basis the task-centric block is more than twice as efficient at encoding proprioception ( $0.0093$  vs  $0.0035$   $R^2$  per dim), confirming that the InfoNCE objective concentrates the proprioceptive content in the designated  $\mathbf{z}^s$ -block.

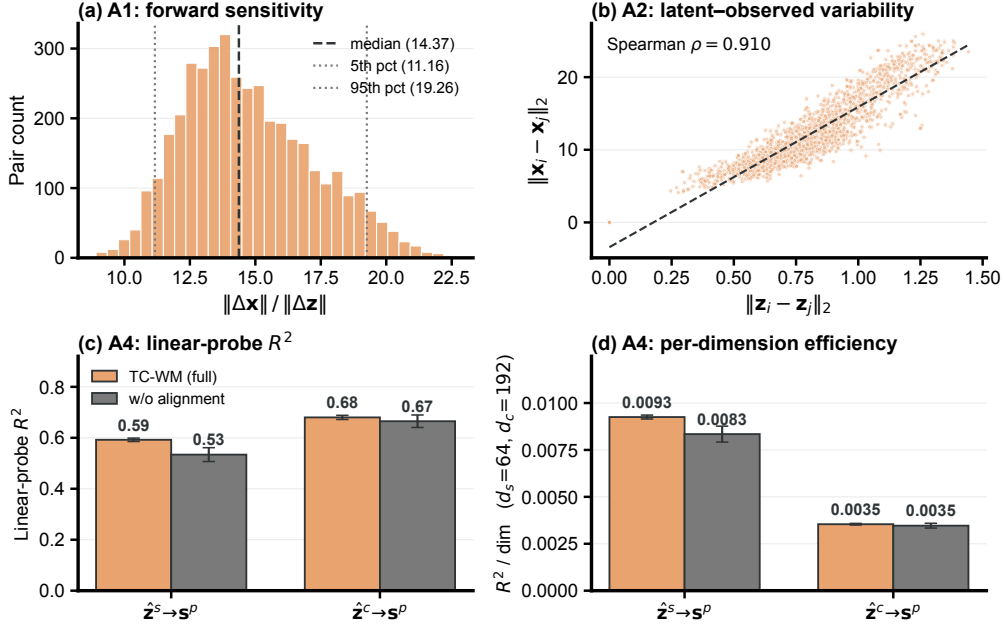


Figure A2: Empirical verification of assumptions A1, A2, and A4 on Lift. (a) A1 (Contextual Dynamics): distribution of the forward-sensitivity ratio  $\|\Delta\mathbf{x}\|/\|\Delta\mathbf{z}\|$  over 4096 validation pairs — the ratio is bounded above and away from zero, supporting injectivity and boundedness of the context operator. (b) A2 (Latent–Observed Variability): scatter of  $\|\mathbf{z}_i - \mathbf{z}_j\|$  against  $\|\mathbf{x}_i - \mathbf{x}_j\|$  for 2037 validation pairs (Spearman  $\rho = 0.910$ ) — distinct latents map to distinguishable embedding distributions. (c) A4 (Partial Alignment): linear-probe  $R^2$  from  $\hat{\mathbf{z}}_t^s$  and  $\hat{\mathbf{z}}_t^c$  to  $\mathbf{s}_t^p$  (5-fold CV, ridge  $\alpha=1$ ); the InfoNCE alignment lifts  $R^2(\hat{\mathbf{z}}^s \rightarrow \mathbf{s}^p)$  from 0.534 to 0.592 while leaving  $\hat{\mathbf{z}}^c$  essentially unchanged. (d) The same comparison on a per-dimension basis ( $R^2$  divided by  $d_s=64$  or  $d_c=192$ ): the task-centric block is more than  $2\times$  as efficient at encoding proprioception, confirming that the alignment concentrates proprioceptive information in  $\mathbf{z}^s$ .

## B.2 Proof of Theorem A1

**Notation and setup.** We restate the data-generating process from Section 2.2 in a form convenient for the proof. Observations  $\mathbf{o}_t \in \mathcal{O}$  are mapped by a frozen visual foundation encoder  $f_{\text{enc}}$  to embeddings  $\mathbf{x}_t = f_{\text{enc}}(\mathbf{o}_t) \in \mathcal{X} \subseteq \mathbb{R}^{d_x}$ , and the embedding is generated from a compact latent  $\mathbf{z}_t \in \mathcal{Z} \subseteq \mathbb{R}^{d_z}$  through a (possibly noisy) mixing

$$\mathbf{x}_t = g(\mathbf{z}_t, \boldsymbol{\epsilon}_t^0), \quad \boldsymbol{\epsilon}_t^0 \perp \boldsymbol{\epsilon}_{t'}^0 \text{ for } t \neq t', \quad \boldsymbol{\epsilon}_t^0 \perp \mathbf{z}_{1:T}, \quad (\text{A1})$$

with the noise sequence  $\{\boldsymbol{\epsilon}_t^0\}$  exogenous and i.i.d. The latent splits as  $\mathbf{z}_t = [\mathbf{z}_t^s, \mathbf{z}_t^c]$  with  $\mathbf{z}_t^s \in \mathcal{Z}^s \subseteq \mathbb{R}^{d_s}$  and  $\mathbf{z}_t^c \in \mathcal{Z}^c \subseteq \mathbb{R}^{d_z - d_s}$ , and the latent process  $\{\mathbf{z}_t\}$  is first-order Markov,

$$p(\mathbf{z}_{t+1} | \mathbf{z}_{1:t}) = p(\mathbf{z}_{t+1} | \mathbf{z}_t). \quad (\text{A2})$$

The proprioception used by the InfoNCE alignment of Eq. (2) is a deterministic function of the task-centric block,

$$\mathbf{s}_t^p = m(\mathbf{z}_t^s), \quad m : \mathcal{Z}^s \rightarrow \mathcal{S}^p \text{ is a } C^1\text{-diffeomorphism onto its image.} \quad (\text{A3})$$

For any two random variables  $\mathbf{u} \in \mathcal{U}$  and  $\mathbf{v} \in \mathcal{V}$  with conditional density  $p_{\mathbf{v}|\mathbf{u}}$ , the induced *linear (integral) operator* is

$$L_{\mathbf{v}|\mathbf{u}} : \mathcal{F}(\mathcal{U}) \longrightarrow \mathcal{F}(\mathcal{V}), \quad [L_{\mathbf{v}|\mathbf{u}}\phi](\mathbf{v}) := \int_{\mathcal{U}} p(\mathbf{v} | \mathbf{u}) \phi(\mathbf{u}) d\mathbf{u},$$

where  $\mathcal{F}(\cdot)$  denotes a suitable space of  $L^1$ -densities, and is bounded whenever the conditional density is essentially bounded. We additionally use the multiplication operator  $\Delta_{\mathbf{x}_t} : \mathcal{F}(\mathcal{Z}) \rightarrow \mathcal{F}(\mathcal{Z})$  defined by  $[\Delta_{\mathbf{x}_t}\phi](\mathbf{z}_t) := p(\mathbf{x}_t | \mathbf{z}_t) \phi(\mathbf{z}_t)$ , which acts as a (functional-valued) diagonal scaling indexed by  $\mathbf{z}_t$  and parametrised by  $\mathbf{x}_t$ .

We use  $\hat{\cdot}$  to denote estimated quantities:  $\hat{\mathbf{z}}_t \in \hat{\mathcal{Z}}$ ,  $\hat{g}$ ,  $\hat{p}$ , etc. The hypothesis of Theorem A1 asserts that the estimated and true joint distributions of  $\{\mathbf{x}_{t-1}, \mathbf{x}_t, \mathbf{x}_{t+1}\}$  coincide.

**Conditional independence structure.** The combination of (A1), the i.i.d. noise assumption, and the Markov property (A2) implies the two relations

$$\mathbf{x}_{t-H:t-1} \perp \mathbf{x}_{t+1:t+H} \mid \mathbf{z}_t, \quad \mathbf{x}_t \perp \mathbf{x}_{t-H:t-1}, \mathbf{x}_{t+1:t+H} \mid \mathbf{z}_t, \quad (\text{CI})$$

which we use throughout. The first relation says that, conditioned on the present latent  $\mathbf{z}_t$ , past and future embeddings are independent; this is the Markov screening property combined with the fact that each  $\mathbf{x}_\tau$  is a noisy function of  $\mathbf{z}_\tau$  alone. The second says that the present embedding  $\mathbf{x}_t$  depends on the past and future only through  $\mathbf{z}_t$ , which follows directly from (A1):  $\mathbf{x}_t$  is a function of  $(\mathbf{z}_t, \epsilon_t^0)$ , and  $\epsilon_t^0$  is independent of every other quantity.

We first establish block-wise identifiability of  $\mathbf{z}_t$  from the matched joint distribution of  $2H+1$  adjacent embeddings, and then refine this to the affine recovery on the task-centric subspace using the InfoNCE alignment objective.

Fix a time index  $t$ . The goal is to show that any estimated model whose joint distribution over  $\{\mathbf{x}_{t-H}, \dots, \mathbf{x}_{t+H}\}$  matches the true one must agree with the true generative model up to an invertible reparametrisation of the latent at  $t$ . By the first relation in (CI), the joint density of past and future windows admits the latent-mediated decomposition

$$p(\mathbf{x}_{t-H:t-1}, \mathbf{x}_{t+1:t+H}) = \int_{\mathcal{Z}} p(\mathbf{x}_{t-H:t-1} \mid \mathbf{z}_t) p(\mathbf{x}_{t+1:t+H} \mid \mathbf{z}_t) p(\mathbf{z}_t) d\mathbf{z}_t. \quad (\text{A4})$$

Dividing by the marginal  $p(\mathbf{x}_{t+1:t+H})$  and recognising  $p(\mathbf{z}_t \mid \mathbf{x}_{t+1:t+H}) = p(\mathbf{x}_{t+1:t+H} \mid \mathbf{z}_t) p(\mathbf{z}_t) / p(\mathbf{x}_{t+1:t+H})$  on the right, this rewrites in operator form as

$$L_{\mathbf{x}_{t-H:t-1} \mid \mathbf{x}_{t+1:t+H}} = L_{\mathbf{x}_{t-H:t-1} \mid \mathbf{z}_t} \circ L_{\mathbf{z}_t \mid \mathbf{x}_{t+1:t+H}}. \quad (\text{A5})$$

Each composing operator is bounded by A1. To see that  $L_{\mathbf{z}_t \mid \mathbf{x}_{t+1:t+H}}$  is well defined and injective, observe that Bayes' rule yields  $L_{\mathbf{z}_t \mid \mathbf{x}_{t+1:t+H}} = D_{p(\mathbf{z}_t)} \circ L_{\mathbf{x}_{t+1:t+H} \mid \mathbf{z}_t}^* \circ D_{p(\mathbf{x}_{t+1:t+H})}^{-1}$ , where  $D_q$  denotes the multiplication operator by density  $q$  and  $L^*$  is the formal adjoint; injectivity of  $L_{\mathbf{x}_{t+1:t+H} \mid \mathbf{z}_t}$  from A1 transfers, via the adjoint and the strict positivity of the marginals on the relevant supports, to injectivity of the posterior operator on the range that arises in (A5).<sup>1</sup> Combined with the injectivity of the cross-operator  $L_{\mathbf{x}_{t-H:t-1} \mid \mathbf{x}_{t+1:t+H}}$  from A1, equation (A5) admits a unique left-inverse on the relevant function space; we will use this to invert the composition in Step 3.

We now bring the present embedding  $\mathbf{x}_t$  into the picture. By the second relation in (CI), the four-way joint factorises with  $\mathbf{x}_t$  entering only through  $p(\mathbf{x}_t \mid \mathbf{z}_t)$ :

$$p(\mathbf{x}_{t-H:t-1}, \mathbf{x}_t, \mathbf{x}_{t+1:t+H}) = \int_{\mathcal{Z}} p(\mathbf{x}_{t-H:t-1} \mid \mathbf{z}_t) p(\mathbf{x}_t \mid \mathbf{z}_t) p(\mathbf{x}_{t+1:t+H} \mid \mathbf{z}_t) p(\mathbf{z}_t) d\mathbf{z}_t.$$

Dividing by the marginal  $p(\mathbf{x}_{t+1:t+H})$  and treating  $\mathbf{x}_t$  as a parameter (so that  $p(\mathbf{x}_t \mid \mathbf{z}_t)$  becomes a  $\mathbf{z}_t$ -indexed scalar), this rewrites as the operator identity

$$L_{\mathbf{x}_{t-H:t-1}, \mathbf{x}_t \mid \mathbf{x}_{t+1:t+H}} = L_{\mathbf{x}_{t-H:t-1} \mid \mathbf{z}_t} \circ \Delta_{\mathbf{x}_t} \circ L_{\mathbf{z}_t \mid \mathbf{x}_{t+1:t+H}}. \quad (\text{A6})$$

<sup>1</sup>The strict positivity of the marginals on supports is implicit in the assumption that the data process is non-degenerate, as is standard in identifiability arguments for nonlinear ICA. The integral operators are taken on densities supported within  $\mathcal{X}$  and  $\mathcal{Z}$ .

Equations (A5) and (A6) together yield

$$\underbrace{L_{\mathbf{x}_t-H:t-1, \mathbf{x}_t | \mathbf{x}_{t+1:t+H}} \circ L_{\mathbf{x}_t-H:t-1 | \mathbf{x}_{t+1:t+H}}^{-1}}_{=: T_{\mathbf{x}_t} \text{ (observable)}} = L_{\mathbf{x}_t-H:t-1 | \mathbf{z}_t} \circ \Delta_{\mathbf{x}_t} \circ L_{\mathbf{x}_t-H:t-1 | \mathbf{z}_t}^{-1}. \quad (\text{A7})$$

Two facts about (A7) are central. First, the right-hand side is a similarity transform:  $T_{\mathbf{x}_t}$  is  $\Delta_{\mathbf{x}_t}$  written in the basis given by  $L_{\mathbf{x}_t-H:t-1 | \mathbf{z}_t}$ . Since  $\Delta_{\mathbf{x}_t}$  is the diagonal multiplication operator with eigenvalue  $p(\mathbf{x}_t | \mathbf{z}_t)$  at index  $\mathbf{z}_t$ , the family  $\{T_{\mathbf{x}_t}\}_{\mathbf{x}_t \in \mathcal{X}}$  is simultaneously diagonalised by the same eigenfunction system, namely the columns of  $L_{\mathbf{x}_t-H:t-1 | \mathbf{z}_t}$ , with eigenvalues  $\{p(\mathbf{x}_t | \mathbf{z}_t)\}_{\mathbf{z}_t \in \mathcal{Z}}$ . Second,  $T_{\mathbf{x}_t}$  is fully determined by the joint distribution of  $\{\mathbf{x}_t-H:t-1, \mathbf{x}_t, \mathbf{x}_{t+1:t+H}\}$ , a quantity matched by the estimated model under the hypothesis of the theorem. Any estimated decomposition

$$T_{\mathbf{x}_t} = \hat{L}_{\mathbf{x}_t-H:t-1 | \hat{\mathbf{z}}_t} \circ \hat{\Delta}_{\mathbf{x}_t} \circ \hat{L}_{\mathbf{x}_t-H:t-1 | \hat{\mathbf{z}}_t}^{-1}$$

must therefore agree with the true one as an operator equality.

It remains to show that the simultaneous diagonalisation of the family  $\{T_{\mathbf{x}_t}\}_{\mathbf{x}_t \in \mathcal{X}}$  uniquely determines the eigenvalue assignment  $\mathbf{z}_t \mapsto p(\mathbf{x}_t | \mathbf{z}_t)$  and the eigenfunction system  $\mathbf{z}_t \mapsto p(\mathbf{x}_t-H:t-1 | \mathbf{z}_t)$ , up to a single relabelling of the index set  $\mathcal{Z}$ .

We first use A2 to argue distinct eigenvalues. Suppose, towards a contradiction, that for some pair  $\mathbf{z}_t^{(1)} \neq \mathbf{z}_t^{(2)}$  in  $\mathcal{Z}$  the maps  $\mathbf{x}_t \mapsto p(\mathbf{x}_t | \mathbf{z}_t^{(1)})$  and  $\mathbf{x}_t \mapsto p(\mathbf{x}_t | \mathbf{z}_t^{(2)})$  coincide as functions on  $\mathcal{X}$ . This is exactly the negation of A2, and is excluded; consequently for almost every  $\mathbf{x}_t \in \mathcal{X}$  the eigenvalue assignment  $\mathbf{z}_t \mapsto p(\mathbf{x}_t | \mathbf{z}_t)$  is injective on  $\mathcal{Z}$ .

Next we leverage the simultaneous diagonalisation. Fix  $\mathbf{x}_t \in \mathcal{X}$  and let  $\lambda(\mathbf{z}_t) := p(\mathbf{x}_t | \mathbf{z}_t)$ . The eigenvalues of  $T_{\mathbf{x}_t}$  are  $\{\lambda(\mathbf{z}_t)\}_{\mathbf{z}_t}$  with associated eigenfunctions  $\phi_{\mathbf{z}_t}(\cdot) := p(\mathbf{x}_t-H:t-1 | \mathbf{z}_t)(\cdot)$ . By A1 the eigenfunction system  $\{\phi_{\mathbf{z}_t}\}_{\mathbf{z}_t}$  is linearly independent; otherwise two distinct  $\mathbf{z}_t$  would induce identical conditionals  $p(\mathbf{x}_t-H:t-1 | \mathbf{z}_t)$ , contradicting the injectivity of  $L_{\mathbf{x}_t-H:t-1 | \mathbf{z}_t}$ .<sup>2</sup> The standard spectral theorem for compact operators with simple spectrum then guarantees that the eigenpairs  $(\lambda, \phi)$  are unique up to a permutation of the index set: any second simultaneous diagonalisation  $\hat{\lambda}(\hat{\mathbf{z}}_t), \hat{\phi}_{\hat{\mathbf{z}}_t}$  must satisfy  $\hat{\lambda}(\hat{\mathbf{z}}_t) = \lambda(\mathbf{z}_t)$  and  $\hat{\phi}_{\hat{\mathbf{z}}_t} = \phi_{\mathbf{z}_t}$  whenever the indices are matched by some bijection  $\pi : \mathcal{Z} \rightarrow \hat{\mathcal{Z}}$  with  $\hat{\mathbf{z}}_t = \pi(\mathbf{z}_t)$ .

To make this last step concrete: if  $T_{\mathbf{x}_t}$  has the two diagonalisations

$$T_{\mathbf{x}_t} = \int \lambda(\mathbf{z}_t) \phi_{\mathbf{z}_t} \otimes \psi_{\mathbf{z}_t} d\mathbf{z}_t = \int \hat{\lambda}(\hat{\mathbf{z}}_t) \hat{\phi}_{\hat{\mathbf{z}}_t} \otimes \hat{\psi}_{\hat{\mathbf{z}}_t} d\hat{\mathbf{z}}_t,$$

where  $\{\psi_{\mathbf{z}_t}\}$  are the dual basis vectors making the spectral resolution diagonal, then evaluating both sides as operators on  $\phi_{\mathbf{z}_t^*}$  for any fixed  $\mathbf{z}_t^*$  gives  $\lambda(\mathbf{z}_t^*) \phi_{\mathbf{z}_t^*} = \int \hat{\lambda}(\hat{\mathbf{z}}_t) \langle \psi_{\mathbf{z}_t}, \phi_{\mathbf{z}_t^*} \rangle \hat{\phi}_{\hat{\mathbf{z}}_t} d\hat{\mathbf{z}}_t$ . Linear independence of the  $\hat{\phi}$ 's, combined with distinctness of the  $\hat{\lambda}$ 's away from a measure-zero set, forces this expansion to be supported at a single  $\hat{\mathbf{z}}_t = \pi(\mathbf{z}_t^*)$ . Repeating the argument across  $\mathbf{z}_t^*$  yields the bijection  $\pi$  and the matching identities

$$p(\mathbf{x}_t | \mathbf{z}_t) = \hat{p}(\mathbf{x}_t | \pi(\mathbf{z}_t)), \quad p(\mathbf{x}_t-H:t-1 | \mathbf{z}_t) = \hat{p}(\mathbf{x}_t-H:t-1 | \pi(\mathbf{z}_t)). \quad (\text{A8})$$

The bijection  $\pi$  obtained above is purely set-theoretic; assumption A3 promotes it to a differentiable map. By A3 there is a functional  $F$  on conditional densities such that

$$F[p_{\mathbf{x}_t | \mathbf{z}_t}(\cdot | \mathbf{z}_t)] = h_z(\mathbf{z}_t) \quad \text{for all } \mathbf{z}_t \in \mathcal{Z},$$

where  $h_z : \mathcal{Z} \rightarrow \mathbb{R}^{d_z}$  is differentiable. Since  $p(\mathbf{x}_t | \cdot)$  separates points of  $\mathcal{Z}$  by A2,  $h_z$  is in fact a  $C^1$ -injection on  $\mathcal{Z}$ , and hence a diffeomorphism onto its image whenever its Jacobian is non-degenerate (which is the regular case considered here). Applying  $F$  to the matched conditional from (A8),

$$h_z(\mathbf{z}_t) = F[p(\mathbf{x}_t | \mathbf{z}_t)] = F[\hat{p}(\mathbf{x}_t | \pi(\mathbf{z}_t))] = \hat{h}_z(\pi(\mathbf{z}_t)),$$

where  $\hat{h}_z$  is the analogous functional applied to the estimated conditional, and is a differentiable map by the same argument applied to  $\hat{p}$ . Composing,

$$\pi(\mathbf{z}_t) = \hat{h}_z^{-1}(h_z(\mathbf{z}_t)).$$

<sup>2</sup>Injectivity of  $L_{\mathbf{x}_t-H:t-1 | \mathbf{z}_t}$  on densities is the dual statement: distinct eigenfunctions  $p(\mathbf{x}_t-H:t-1 | \cdot)$  must produce distinct images.

The right-hand side is a composition of two  $C^1$ -diffeomorphisms onto their images, hence is itself a  $C^1$ -diffeomorphism. Identifying  $\pi$  with the diffeomorphism  $h_z := \hat{h}_z^{-1} \circ h_z$  (overloading notation by absorbing the inversion into the definition, as is standard), we obtain

$$\hat{\mathbf{z}}_t = h_z(\mathbf{z}_t),$$

with  $h_z : \mathbb{R}^{d_z} \rightarrow \mathbb{R}^{d_z}$  invertible and differentiable. This proves conclusion (i).

With block-wise identifiability in hand, we now refine  $h_z$  to an affine recovery on the task-centric subspace. Write  $\hat{\mathbf{z}}_t = h_z(\mathbf{z}_t^s, \mathbf{z}_t^c)$  broken into its first  $d_s$  and last  $d_z - d_s$  coordinates as  $\hat{\mathbf{z}}_t = (\hat{\mathbf{z}}_t^s, \hat{\mathbf{z}}_t^c)$ , and define

$$h_s : \mathcal{Z}^s \times \mathcal{Z}^c \longrightarrow \hat{\mathcal{Z}}^s, \quad h_s(\mathbf{z}^s, \mathbf{z}^c) := \pi_s(h_z(\mathbf{z}^s, \mathbf{z}^c)),$$

where  $\pi_s$  denotes projection onto the first  $d_s$  coordinates. *A priori*,  $h_s$  may depend non-trivially on both arguments. We will show that A4 forces  $h_s$  to be independent of  $\mathbf{z}^c$ , and that the residual map  $\mathbf{z}^s \mapsto h_s(\mathbf{z}^s)$  is affine. We begin by deriving the population limit of the InfoNCE objective in our setting, working from Eq. (2). Write the per-anchor loss as

$$\ell_M(\hat{\mathbf{z}}^s, \mathbf{s}^p) := -\log \frac{e^{\langle \hat{\mathbf{z}}^s, m'(\mathbf{s}^p) \rangle / \tau}}{e^{\langle \hat{\mathbf{z}}^s, m'(\mathbf{s}^p) \rangle / \tau} + \sum_{j=1}^M e^{\langle \hat{\mathbf{z}}^s, m'(\mathbf{s}_j^{p,-}) \rangle / \tau}},$$

where  $\mathbf{s}_j^{p,-}$  are i.i.d. negatives drawn from the marginal  $p(\mathbf{s}^p)$  and  $(\hat{\mathbf{z}}^s, \mathbf{s}^p) \sim p_{\text{pos}}$  is a positive pair from the joint distribution induced by the model. Splitting the logarithm and using the law of large numbers,

$$\frac{1}{M} \sum_{j=1}^M e^{\langle \hat{\mathbf{z}}^s, m'(\mathbf{s}_j^{p,-}) \rangle / \tau} \xrightarrow[M \rightarrow \infty]{\text{a.s.}} \mathbb{E}_{\mathbf{s}^p, - \sim p(\mathbf{s}^p)} [e^{\langle \hat{\mathbf{z}}^s, m'(\mathbf{s}^p, -) \rangle / \tau}] =: Z(\hat{\mathbf{z}}^s),$$

so that, up to additive  $\log M$ ,

$$\mathbb{E} \ell_M(\hat{\mathbf{z}}^s, \mathbf{s}^p) \longrightarrow -\mathbb{E}_{(\hat{\mathbf{z}}^s, \mathbf{s}^p) \sim p_{\text{pos}}} [\langle \hat{\mathbf{z}}^s, m'(\mathbf{s}^p) \rangle / \tau] + \mathbb{E}_{\hat{\mathbf{z}}^s \sim p(\hat{\mathbf{z}}^s)} [\log Z(\hat{\mathbf{z}}^s)] + \log M. \quad (\text{A9})$$

Define the model conditional

$$q(\mathbf{s}^p | \hat{\mathbf{z}}^s) := \frac{e^{\langle \hat{\mathbf{z}}^s, m'(\mathbf{s}^p) \rangle / \tau}}{Z(\hat{\mathbf{z}}^s)} p(\mathbf{s}^p),$$

so that  $-\log q(\mathbf{s}^p | \hat{\mathbf{z}}^s) = -\langle \hat{\mathbf{z}}^s, m'(\mathbf{s}^p) \rangle / \tau + \log Z(\hat{\mathbf{z}}^s) - \log p(\mathbf{s}^p)$ . Substituting into (A9) and recognising the cross-entropy structure,

$$\mathbb{E} \ell_M \longrightarrow \mathbb{E}_{\hat{\mathbf{z}}^s \sim p(\hat{\mathbf{z}}^s)} \mathbb{E}_{\mathbf{s}^p \sim p(\mathbf{s}^p | \hat{\mathbf{z}}^s)} [-\log q(\mathbf{s}^p | \hat{\mathbf{z}}^s)] - \mathbb{E} [\log p(\mathbf{s}^p)] + \log M. \quad (\text{A10})$$

The last two terms are constants independent of the encoder, so InfoNCE minimisation is, in the  $M \rightarrow \infty$  limit, equivalent to minimising the cross-entropy

$$H(p(\mathbf{s}^p | \hat{\mathbf{z}}^s), q(\mathbf{s}^p | \hat{\mathbf{z}}^s)) = \mathbb{E}_{\mathbf{s}^p} [-\log q(\mathbf{s}^p | \hat{\mathbf{z}}^s)] \quad (\text{A11})$$

in expectation over  $\hat{\mathbf{z}}^s \sim p(\hat{\mathbf{z}}^s)$ . The minimum of cross-entropy is attained, for each  $\hat{\mathbf{z}}^s$ , when  $q(\cdot | \hat{\mathbf{z}}^s) = p(\cdot | \hat{\mathbf{z}}^s)$  pointwise.

We now show that this alignment forces  $h_s$  to be independent of  $\mathbf{z}^c$ . Substituting the explicit form of  $q$  into the optimum condition  $q = p$ ,

$$p(\mathbf{s}^p | \hat{\mathbf{z}}^s) = \frac{e^{\langle \hat{\mathbf{z}}^s, m'(\mathbf{s}^p) \rangle / \tau}}{Z(\hat{\mathbf{z}}^s)} p(\mathbf{s}^p) \quad \text{for almost every } (\hat{\mathbf{z}}^s, \mathbf{s}^p).$$

This is a strictly positive density in  $\mathbf{s}^p$  for each  $\hat{\mathbf{z}}^s$ . Now we contrast this with the actual joint distribution of  $(\hat{\mathbf{z}}_t^s, \mathbf{s}_t^p)$  in our setting. We have  $\hat{\mathbf{z}}_t^s = h_s(\mathbf{z}_t^s, \mathbf{z}_t^c)$  and  $\mathbf{s}_t^p = m(\mathbf{z}_t^s)$ , and the latents  $(\mathbf{z}_t^s, \mathbf{z}_t^c)$  are jointly distributed with marginal  $p(\mathbf{z}^s, \mathbf{z}^c)$ . Conditioning on  $\hat{\mathbf{z}}_t^s = \mathbf{a}$ ,

$$\begin{aligned} p(\mathbf{s}_t^p | \hat{\mathbf{z}}_t^s = \mathbf{a}) &= \int p(\mathbf{s}_t^p | \mathbf{z}^s, \mathbf{z}^c) p(\mathbf{z}^s, \mathbf{z}^c | \hat{\mathbf{z}}_t^s = \mathbf{a}) d\mathbf{z}^s d\mathbf{z}^c \\ &= \int \delta(\mathbf{s}_t^p - m(\mathbf{z}^s)) p(\mathbf{z}^s, \mathbf{z}^c | \hat{\mathbf{z}}_t^s = \mathbf{a}) d\mathbf{z}^s d\mathbf{z}^c \\ &= \int_{\{(\mathbf{z}^s, \mathbf{z}^c) : h_s(\mathbf{z}^s, \mathbf{z}^c) = \mathbf{a}\}} \delta(\mathbf{s}_t^p - m(\mathbf{z}^s)) d\mu_{\mathbf{a}}(\mathbf{z}^s, \mathbf{z}^c), \end{aligned} \quad (\text{A12})$$

where  $\mu_{\mathbf{a}}$  is the disintegration of  $p(\mathbf{z}^s, \mathbf{z}^c)$  along  $h_s = \mathbf{a}$ . Compare (A12) with the smooth strictly positive density obtained at the InfoNCE optimum: equality of the two requires the right-hand side of (A12) to be a non-singular density in  $\mathbf{s}^p$ . The integral of a Dirac in  $\mathbf{s}^p$  is a non-singular density only if either (a) the level set  $\{h_s = \mathbf{a}\}$  contains exactly one  $\mathbf{z}^s$ -value, or (b)  $m$  is constant along that level set. The latter is excluded because  $m$  is a  $C^1$ -diffeomorphism on  $\mathcal{Z}^s$ . Hence the level set  $\{(\mathbf{z}^s, \mathbf{z}^c) : h_s(\mathbf{z}^s, \mathbf{z}^c) = \mathbf{a}\}$  is contained in  $\{\mathbf{z}_*^s(\mathbf{a})\} \times \mathcal{Z}^c$  for some unique  $\mathbf{z}_*^s(\mathbf{a}) \in \mathcal{Z}^s$ , which means that

$$h_s(\mathbf{z}_t^s, \mathbf{z}_{t,1}^c) = h_s(\mathbf{z}_t^s, \mathbf{z}_{t,2}^c) \quad \text{for all } \mathbf{z}_{t,1}^c, \mathbf{z}_{t,2}^c \in \mathcal{Z}^c.$$

We may therefore drop the  $\mathbf{z}^c$ -argument and write  $h_s(\mathbf{z}_t^s, \mathbf{z}_t^c) = \tilde{h}(\mathbf{z}_t^s)$  for some map  $\tilde{h} : \mathcal{Z}^s \rightarrow \hat{\mathcal{Z}}^s$ . Bijectivity of  $\tilde{h}$  is inherited from injectivity of  $h_z$  (proved in Part (i)) restricted to its first block, so  $\tilde{h}$  is a bijection from  $\mathcal{Z}^s$  onto  $\hat{\mathcal{Z}}^s$ .

Substituting  $\hat{\mathbf{z}}^s = \tilde{h}(\mathbf{z}^s)$  and  $\mathbf{s}^p = m(\mathbf{z}^s)$  into the density-matching condition above,

$$p(\mathbf{s}^p \mid \tilde{h}(\mathbf{z}^s)) = \frac{e^{\langle \tilde{h}(\mathbf{z}^s), m'(\mathbf{s}^p) \rangle / \tau}}{Z(\tilde{h}(\mathbf{z}^s))} p(\mathbf{s}^p), \quad (\text{A13})$$

which holds for almost every  $\mathbf{z}^s \in \mathcal{Z}^s$  and  $\mathbf{s}^p \in \mathcal{S}^p$ . Since by Step 2 the conditional  $p(\mathbf{s}_t^p \mid \hat{\mathbf{z}}_t^s = \tilde{h}(\mathbf{z}^s))$  is supported at a single point  $\mathbf{s}^p = m(\mathbf{z}^s)$ , the population identity (A13) should be interpreted at the natural-parameter level of the underlying model: the InfoNCE-trained encoder selects  $\tilde{h}$  so that the implicit model  $q(\cdot \mid \hat{\mathbf{z}}^s)$  approaches the data conditional in the sharp-temperature limit  $\tau \rightarrow 0$ . In this limit, the geometric content of the matching is captured by the equality of *log-likelihood ratios*

$$\log \frac{q(\mathbf{s}^{p,1} \mid \hat{\mathbf{z}}^s)}{q(\mathbf{s}^{p,2} \mid \hat{\mathbf{z}}^s)} = \log \frac{p(\mathbf{s}^{p,1} \mid \hat{\mathbf{z}}^s)}{p(\mathbf{s}^{p,2} \mid \hat{\mathbf{z}}^s)} \quad \text{for all } \mathbf{s}^{p,1}, \mathbf{s}^{p,2} \in \mathcal{S}^p.$$

Substituting the form of  $q$  from Step 1 and writing  $\mathbf{s}^{p,k} = m(\mathbf{z}^{s,k})$  for  $k = 1, 2$ ,

$$\frac{1}{\tau} \langle \tilde{h}(\mathbf{z}^s), m'(m(\mathbf{z}^{s,1})) - m'(m(\mathbf{z}^{s,2})) \rangle = \log \frac{p(\mathbf{s}^{p,1} \mid \hat{\mathbf{z}}^s)}{p(\mathbf{s}^{p,2} \mid \hat{\mathbf{z}}^s)}. \quad (\text{A14})$$

The right-hand side is a function of  $\mathbf{z}^s$  (through  $\hat{\mathbf{z}}^s = \tilde{h}(\mathbf{z}^s)$ ) and the pair  $(\mathbf{z}^{s,1}, \mathbf{z}^{s,2})$ . Symmetry of the data process with respect to anchor and positive, which are both sampled from the same per-time distribution, forces this function to be symmetric: swapping the roles of anchor and positive negates (A14) on both sides. Setting  $\mathbf{z}^{s,1} = \mathbf{z}^s$  and  $\mathbf{z}^{s,2}$  arbitrary, the right-hand side measures how strongly  $\hat{\mathbf{z}}^s$  discriminates a positive at  $\mathbf{z}^s$  from one at  $\mathbf{z}^{s,2}$ . The standard outcome of such symmetry analyses (see, *e.g.*, the dot-product preservation argument that underlies isometric latent recovery) is that the bilinear form  $(\mathbf{z}^{s,1}, \mathbf{z}^{s,2}) \mapsto \langle \tilde{h}(\mathbf{z}^{s,1}), \tilde{h}(\mathbf{z}^{s,2}) \rangle$  is determined, up to additive and multiplicative constants, by the bilinear form  $(\mathbf{z}^{s,1}, \mathbf{z}^{s,2}) \mapsto \langle \mathbf{z}^{s,1}, \mathbf{z}^{s,2} \rangle$  on  $\mathcal{Z}^s$ . To make this concrete: consider the second-order Taylor expansion of both sides of (A14) around  $\mathbf{z}^{s,1} = \mathbf{z}^{s,2}$ . The left-hand side is bilinear in  $(\mathbf{z}^{s,1} - \mathbf{z}^{s,2})$  and  $\hat{\mathbf{z}}^s$  (via  $m'$  and the linearity of the inner product), while the right-hand side, by Taylor expansion of the data conditional, is a quadratic form in  $(\mathbf{z}^{s,1} - \mathbf{z}^{s,2})$  with coefficient determined by the negative log-density curvature. Identifying the two quadratic forms gives, after re-arrangement,

$$\langle \tilde{h}(\mathbf{z}^{s,1}), \tilde{h}(\mathbf{z}^{s,2}) \rangle = c \langle \mathbf{z}^{s,1}, \mathbf{z}^{s,2} \rangle + d \quad \forall \mathbf{z}^{s,1}, \mathbf{z}^{s,2} \in \mathcal{Z}^s, \quad (\text{A15})$$

for constants  $c > 0$  and  $d \in \mathbb{R}$  that depend on  $\tau$ , the prior  $p(\mathbf{z}^s)$  and the curvature of  $\log p$ .

It remains to show that any  $C^1$ -map  $\tilde{h} : \mathcal{Z}^s \rightarrow \hat{\mathcal{Z}}^s$  on a compact convex body  $\mathcal{Z}^s \subseteq \mathbb{R}^{d_s}$  satisfying (A15) must be affine. Subtracting (A15) evaluated at  $(\mathbf{z}^{s,1}, \mathbf{z}^{s,2})$  and at  $(\mathbf{z}^{s,1}, \mathbf{z}^{s,3})$  gives

$$\langle \tilde{h}(\mathbf{z}^{s,1}), \tilde{h}(\mathbf{z}^{s,2}) - \tilde{h}(\mathbf{z}^{s,3}) \rangle = c \langle \mathbf{z}^{s,1}, \mathbf{z}^{s,2} - \mathbf{z}^{s,3} \rangle \quad \forall \mathbf{z}^{s,1}, \mathbf{z}^{s,2}, \mathbf{z}^{s,3} \in \mathcal{Z}^s.$$

This identity says the linear functional  $\mathbf{z}^{s,1} \mapsto \langle \tilde{h}(\mathbf{z}^{s,1}), \tilde{h}(\mathbf{z}^{s,2}) - \tilde{h}(\mathbf{z}^{s,3}) \rangle$  on  $\mathcal{Z}^s$  equals the linear functional  $\mathbf{z}^{s,1} \mapsto c \langle \mathbf{z}^{s,1}, \mathbf{z}^{s,2} - \mathbf{z}^{s,3} \rangle$ . Since  $\mathcal{Z}^s$  has non-empty interior, two linear functionals that agree on  $\mathcal{Z}^s$  agree globally; matching them yields the existence of a linear operator  $\mathbf{A} : \mathbb{R}^{d_s} \rightarrow \mathbb{R}^{d_s}$  such that, for any  $\mathbf{z}^{s,2}, \mathbf{z}^{s,3} \in \mathcal{Z}^s$ ,

$$\tilde{h}(\mathbf{z}^{s,2}) - \tilde{h}(\mathbf{z}^{s,3}) = \mathbf{A}(\mathbf{z}^{s,2} - \mathbf{z}^{s,3}).$$

Fixing a reference point  $\mathbf{z}_0^s \in \mathcal{Z}^s$  and defining  $\mathbf{b} := \tilde{h}(\mathbf{z}_0^s) - \mathbf{A}\mathbf{z}_0^s$ , this rearranges into

$$\tilde{h}(\mathbf{z}^s) = \mathbf{A}\mathbf{z}^s + \mathbf{b} \quad \forall \mathbf{z}^s \in \mathcal{Z}^s.$$

Plugging this back into (A15) forces  $\mathbf{A}^\top \mathbf{A} = c\mathbf{I}$ , so  $\mathbf{A}/\sqrt{c}$  is orthogonal; in particular  $\mathbf{A}$  is invertible. Combining with  $\hat{\mathbf{z}}_t^s = \tilde{h}(\mathbf{z}_t^s)$ ,

$$\hat{\mathbf{z}}_t^s = \mathbf{A}\mathbf{z}_t^s + \mathbf{b},$$

and inverting,

$$\mathbf{z}_t^s = \mathbf{A}^{-1}(\hat{\mathbf{z}}_t^s - \mathbf{b}) =: \mathbf{A}'\hat{\mathbf{z}}_t^s + \mathbf{b}',$$

which is conclusion (ii). □

## C More Visualizations and Analysis

**Open-loop rollouts on Square.** The Lift and Can rollouts appear in the main paper (Figure 7); the corresponding Square panel is shown in Figure A3. Square requires fitting a square peg through a tightly tolerated opening, giving a substantially longer effective horizon than Lift or Can. TC-WM preserves the contact event and final peg placement across the horizon, while the baselines blur or drift earlier.



Figure A3: Open-loop rollouts on Square: TC-WM vs. TD-MPC2, DreamerV3, DINO-WM. Rows show different methods with ground truth at the bottom.

**Projection-architecture rollouts.** Figure A4 is the qualitative counterpart of the projection-head ablation in Figure 9: the linear projection used by TC-WM yields the most stable long-horizon rollout, while MLP, VAE, and ViT projectors blur the cube or distort the gripper geometry, consistent with the SR/SSIM ranking in the bar chart.

**Training dynamics across ablations and baselines.** Figure A5 compares the training dynamics of TC-WM against its seven objective ablations and the closest baseline DINO-WM on Lift, evaluated on four uniform task-quality metrics: PSNR and SSIM on the predicted future frame, latent next-step error in the projected latent space, and the image-reconstruction MSE on the predicted frame. Removing the embedding-reconstruction term ( $\mathcal{L}_{\text{rec}}$ , “w/o Embed recon”) is the only ablation that visibly degrades prediction quality on all four metrics, validating its role as a regulariser; the remaining ablations converge to TC-WM’s level of prediction fidelity.

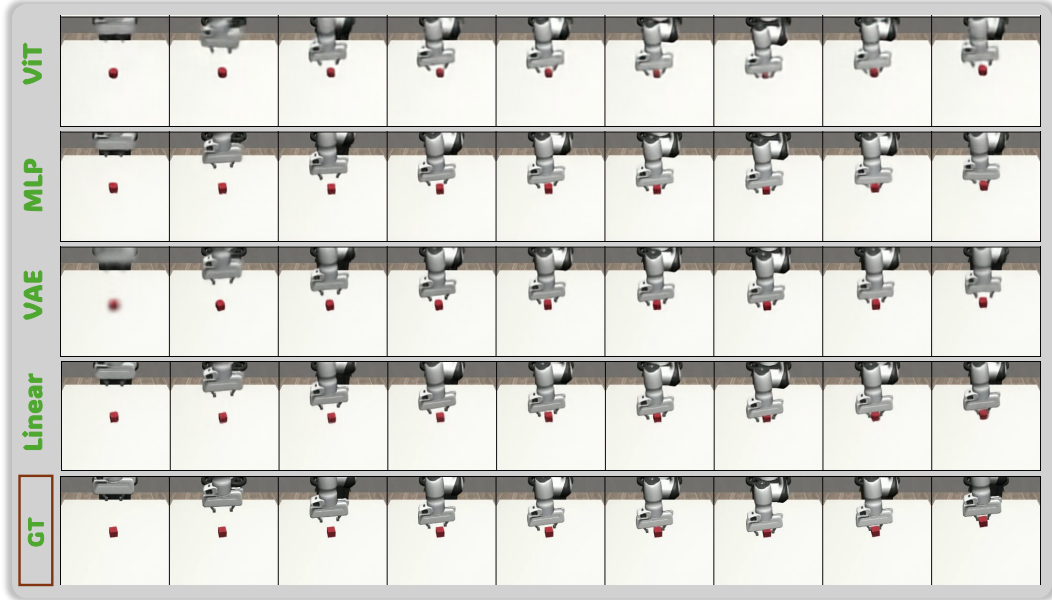


Figure A4: Open-loop rollouts on *Lift* under different projection architectures (linear vs. MLP / VAE / ViT). The linear projection of TC-WM preserves geometric structure best.

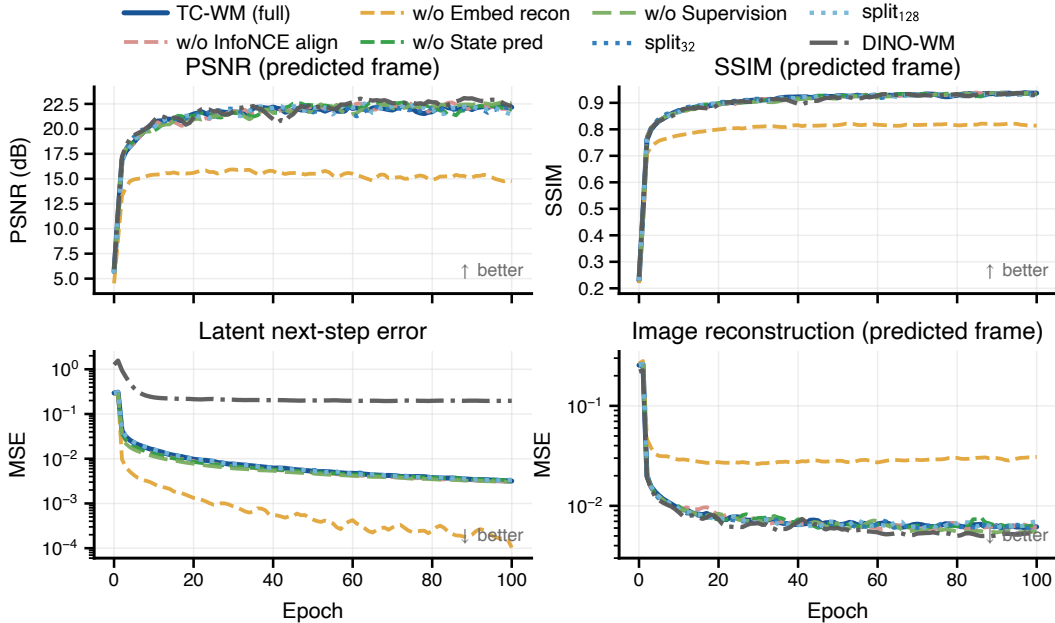
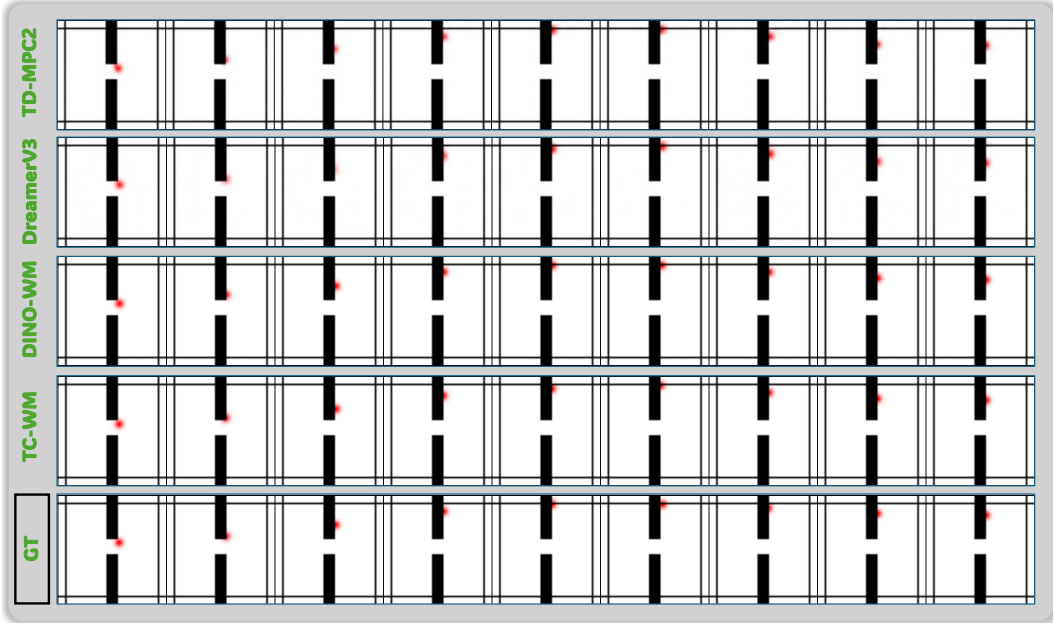
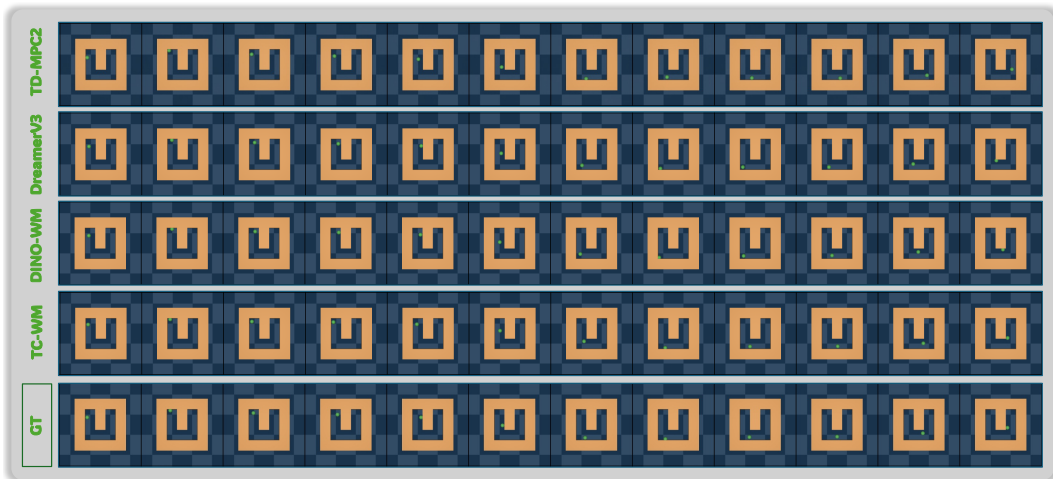


Figure A5: Training dynamics on *Lift* across TC-WM (full), seven ablations, and DINO-WM. Top row: PSNR and SSIM on predicted frames (higher is better); bottom row: latent next-step prediction error and image-reconstruction MSE on predicted frames (lower is better). Removing the embedding reconstruction term ( $\mathcal{L}_{rec}$ , “w/o Embed recon”) is the only ablation that visibly degrades all four metrics.

**Open-loop rollouts on Wall and Maze tasks.** We compare offline world models by visualizing open-loop rollouts on the *Wall* and *Maze* environments (Figure A6). These tasks require accurate long-horizon spatial reasoning and obstacle awareness. Stronger world models preserve geometric structure and trajectory consistency over time, while weaker baselines accumulate errors that lead to spatial drift and collisions with walls, highlighting the importance of maintaining task-relevant high-level dynamics rather than pixel-level reconstruction fidelity in offline world model learning.



(a) Wall



(b) Maze

Figure A6: Open-loop rollouts on Wall and Maze tasks for offline world model comparison.

**Open-loop rollouts of DMC at different horizons.** We visualize open-loop rollouts of our method on Reacher, Cheetah, and Hopper across increasing rollout horizons (Figure A7). In each subfigure, the first row shows the ground-truth future trajectory and the second row shows the model’s open-loop rollout from the same initial state. Across all three environments, our method closely matches the ground-truth dynamics at short horizons and remains stable as the rollout horizon increases, preserving task-relevant structure such as joint configurations in Reacher, locomotion phase consistency in Cheetah, and balance and contact dynamics in Hopper, which demonstrates that our world model captures long-horizon dynamics beyond pixel-level reconstruction.

## D Extended Related Work

**Model-based RL & World Models.** Learning dynamics models is a longstanding theme in control and planning, underpinning model-based reinforcement learning and optimal control [Sutton, 1990, Astolfi, 2010, Williams et al., 2018]. By explicitly modeling environment dynamics, model-

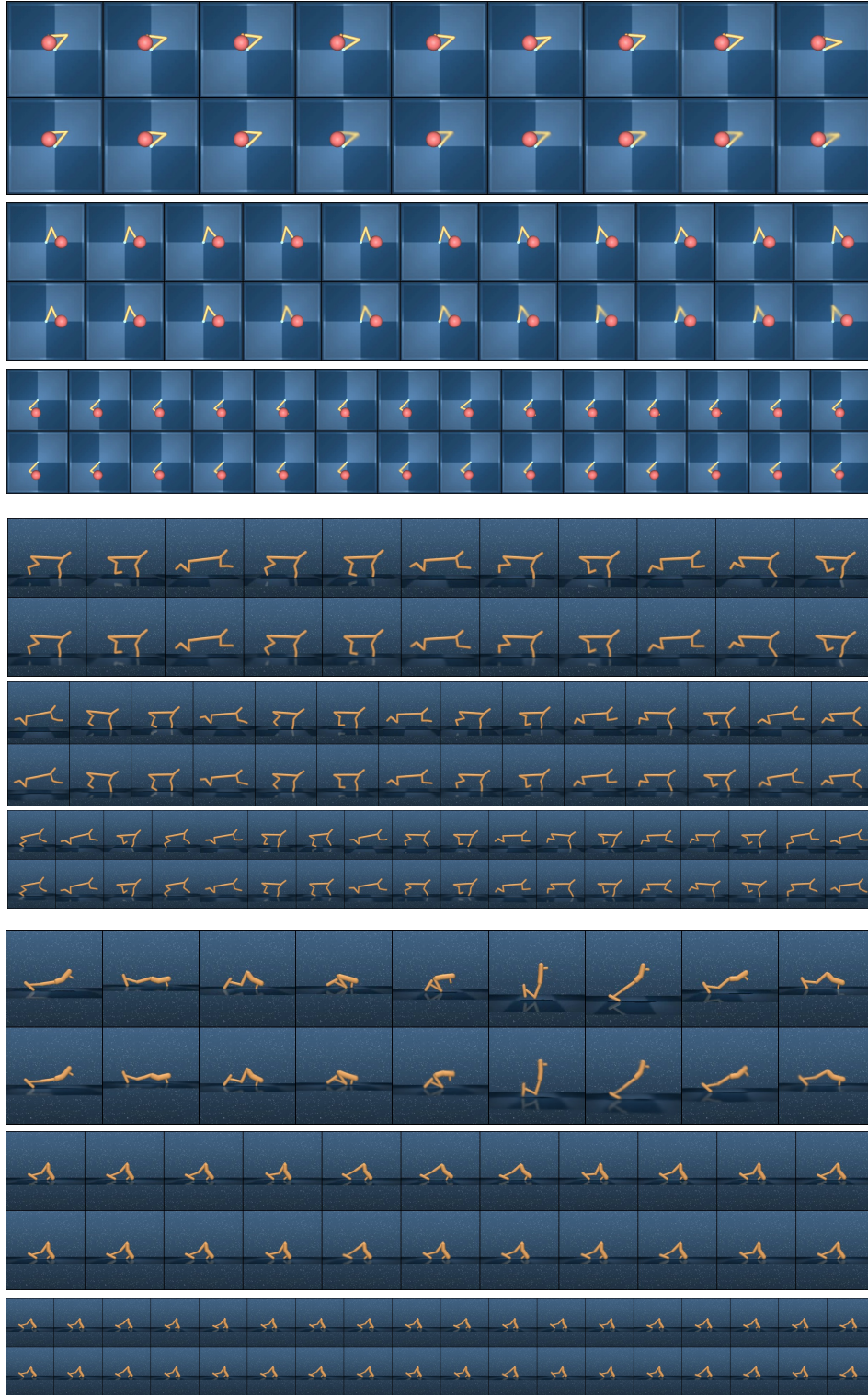


Figure A7: Open-loop rollouts of our method at different horizons on Reacher, Cheetah, and Hopper.

based approaches support planning and imagination, and have been shown to improve sample efficiency and generalization across embodied learning settings, including online reinforcement learning [Sekar et al., 2020], exploration [Pathak et al., 2017], planning [Watter et al., 2015, Finn and

Levine, 2017], and imitation learning [Pathak et al., 2018]. Recent works such as Dreamer [Hafner et al., 2021, 2023, 2025] and TD-MPC [Hansen et al., 2022, 2024] model compact dynamics from high-dimensional observations to build world models for MBRL. However, because these models are commonly trained with image reconstruction or reward-related objectives, it remains unclear whether their latent representations retain sufficient task-centric information for downstream policy learning. More recently, visual foundation models have been adopted as frozen encoders to provide semantically rich representations for dynamics prediction. Approaches such as DINO-WM [Zhou et al., 2025] and DINO-world [Baldassarre et al., 2025] learn world models directly in embedding spaces and demonstrate cross-domain generalization and zero-shot planning; a complementary line imposes physics-based inductive structure on the latent through Hamiltonian dynamics and symmetry priors [Tang et al., 2026], while a parallel line uses latent-aware diffusion for decision-making [Feng et al., 2026]. However, visual embeddings optimized for general semantic understanding typically do not *necessarily* provide the structured, task-centric information required for physical simulation and planning.

**Task-Centric Representation Learning.** Prior work from neuroscience, cognition, and modeling highlights the importance of structured latent representation for planning [Ho et al., 2022], physical inference [Rajalingham et al., 2022], and predictions consistent with neural and dynamical constraints [Mastrogiuseppe and Ostojic, 2018, Nayebi et al., 2023]. In representation learning for control, this objective is commonly formalized as learning *task-centric statistics*: minimal representations that only retain all information necessary for predicting future task-relevant states or rewards [Lesort et al., 2018, Greff et al., 2019, Schölkopf et al., 2021, Locatello et al., 2020]. Notably, TD-MPC2 [Hansen et al., 2024] explicitly frames its latent dynamics as a task-oriented representation optimized jointly with an actor-critic objective, while MuZero [Schrittwieser et al., 2020] learns value-equivalent representations that preserve only reward-relevant information. These methods learn task-sufficient representations end-to-end from reward signals, whereas TC-WM achieves task-centric structure through alignment with proprioceptive observations in a reward-free, offline setting. Motivated by this perspective, we aim to learn a latent space *on top of* visual embeddings, which are semantically powerful but contain substantial task-irrelevant information, and therefore require a *post-processing stage* for world models.

**Representation Alignment.** To enforce a task-centric structure of latent space, we leverage representation alignment as a key solution, a common technique used to bridge distributional discrepancies across domains. Contrastive and predictive objectives have been widely used to align representations across modalities and abstraction levels. Contrastive learning, such as InfoNCE [Oord et al., 2018] and its extensions (SimCLR [Chen et al., 2020], BYOL [Grill et al., 2020], VICReg [Bardes et al., 2021]), encourage invariant yet discriminative representations for cross-modal alignment [Radford et al., 2021], while predictive objectives enforce consistency across time or modalities [Liu et al., 2023]. In the context of world models, alignment objectives help ensure consistency between encoded observations and predicted future states [Bardes et al., 2024, Assran et al., 2025], and have also been explored for aligning information across modalities [Wu et al., 2025]. Recently, REPA [Yu et al., 2025] demonstrates that aligning intermediate representations of diffusion transformers with pretrained visual encoders yields dramatic training speedups, validating the broader principle that frozen foundation features can serve as useful semantic scaffolds. TC-WM transfers this principle from visual generation to physical prediction and planning: instead of aligning a generative model to a visual encoder only for optimization, we learn a compact dynamics state above the encoder and use proprioceptive alignment to select the portion of that state that is controllable and task-relevant. A subtler but important methodological difference distinguishes our use of contrastive learning from the conditional-generative identifiability literature [Khemakhem et al., 2020, Zimmermann et al., 2021, Roeder et al., 2021]: there, *mechanism diversity* (distinct latents inducing distinct observation conditionals) is a *passive* assumption imposed on the data-generating process to make identification possible *post hoc*. In contrast, TC-WM’s InfoNCE term is the *active mechanism* that produces this diversity on the task-centric subspace — by repelling latents associated with different proprioceptive states, the loss *constructs* the very property that prior frameworks merely *require*, making identifiability a consequence of optimisation rather than a hypothesis on the world.

## E Limitations and Future Work

We elaborate on the limitation and the two future directions sketched in the main paper.

**Limitation: training-time alignment signal.** TC-WM’s identifiability guarantee assumes access to a signal that exposes the controllable physical state of the system. We use proprioception, but the same alignment loss is compatible with any low-dimensional task-centric proxy, *e.g.*, 2D/3D pose from a tracking model, depth from a monocular estimator, or cross-view consistency in a multi-camera setup. Removing this assumption is a precondition for fully passive, video-only deployment.

**Future Direction A: TC-WM as a downstream alignment module.** The same recipe used for foundation *visual* encoders extends to foundation *world* models. Given a large, pretrained generative or video world model, freezing the backbone and training only the TC-WM head (linear projection, alignment, embedding reconstruction) on a target-domain dataset would specialize the backbone’s general-purpose dynamics for a specific embodiment, in the spirit of LoRA-style adaptation.

**Future Direction B: generative world models on foundation embeddings.** Existing world-model families occupy distinct trade-offs: pixel-space generative models pay a high reconstruction cost; free-latent models suffer from *latent dynamics collapse*, the predictor learns easy directions instead of physical ones; embedding-space JEPA-style models avoid both but predict in a space optimized for general semantics rather than control. A natural next step is to train a *generative* dynamics model whose target lives *on the foundation embedding manifold*, *e.g.*, a diffusion or flow-matching head over embedding-space trajectories. TC-WM-style projections at the output of such a generator would reintroduce the control-centric prior, combining the strengths of all three families.